Formation of Solid Solutions beyond Solubility Limits in Perovskite-type Oxides by 'Sputter-Anneal' Method

Miho Ako

Domain of Materials and Bioscience,

Graduate School of Science and Technology,

Gunma University

Contents

Chapter 1. General Introduction

1.1. Structure and application of ABO_3 perovskite-type materials

Perovskite-type oxides are very important materials with a general formula of ABO_3 [1-4]. Originally, the mineral of $CaTiO_3$ found out in the Ural Mountains in 1839 was named 'perovskite' after Russian mineralogist L. A. Perovski, and this name is lent to all compounds having the same crystal structure [1-2]. A unit cell of the perovskite-type oxide having a cubic structure is shown in Fig. 1.1 [3,4]. As exhibited in Fig. 1.1(a), it contains A atoms at the corners of the cube, B atom at the body center, and oxygen is at the center of each face. When the B atoms are taken at the corner as in Fig. 1.1(b), the A atom appears at the center and O atoms are located at the mid-point of each edge [1,3]. The coordination environment of each atom is seen in the figure, and interatomic distances can be calculated rather easily by the simple geometry. The distance between the body-centered B atom and octahedrally coordinating oxygen in Fig. 1.1(a), L(B−O), is equal to half of the lattice constant a., i.e., $L(\mathrm{B-O}) = a / 2$. A atom in the cube center in Fig. 1.1(b) is equidistant from all twelve oxygens at edge center positions, and the distance L(A−O) equals half the diagonal of any cell face, i.e., $L(\mathrm{A-O}) = a / \sqrt{2}$ [1,5-7].

Goldschmidt had built the foundation of the crystal chemistry of perovskite-type oxides through extensive syntheses. Based on the foundation, Roy developed the crystal chemistry of perovskites involving multiple ion substitution [8-10]. Roy *et al*. produced

many derivatives on the A site, B site and mixed [8]. A part of Roy's work about perovskite-type compounds in 1954 is shown in Fig. 1.2 [10]. After that, the perovskite-type oxides, ABO_3, were investigated in various fields and have been revealed that they can produce an incredibly wide array of phases with totally different functions [11]. For example, as shown in Fig. 1.3, capacitor [12-14], piezoelectric or pyroelectric devices [15,16], catalysts [17-19], solid oxide fuel cells [20,21], and so on [22-25].

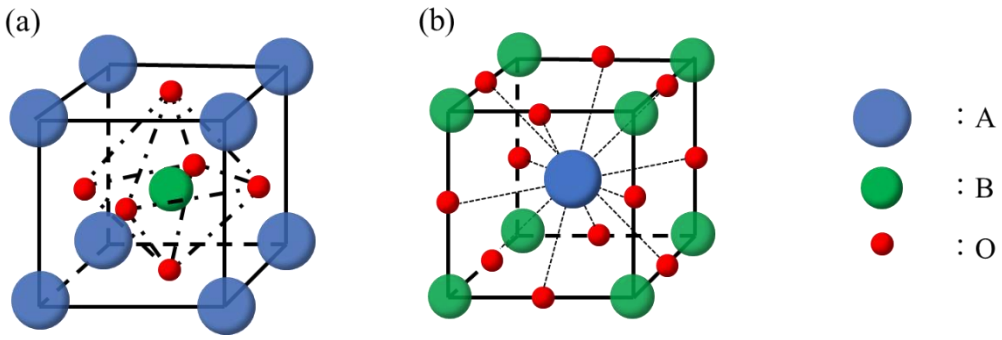

Fig. 1.1　Unit cell of the ABO_3 perovskite structure in two different views. The B atom is at the center of octahedra composed of six oxygen atoms (a), and the A atom has neighboring twelve oxygens (b).

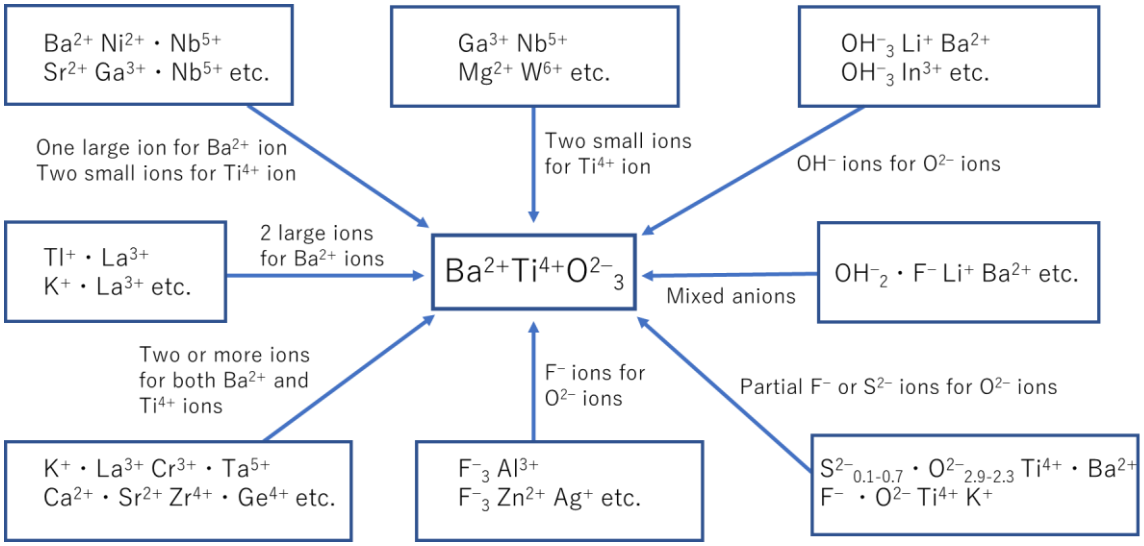

Fig. 1.2 Crystal chemistry of multiple-ion substitution in perovskite-type oxides [10].

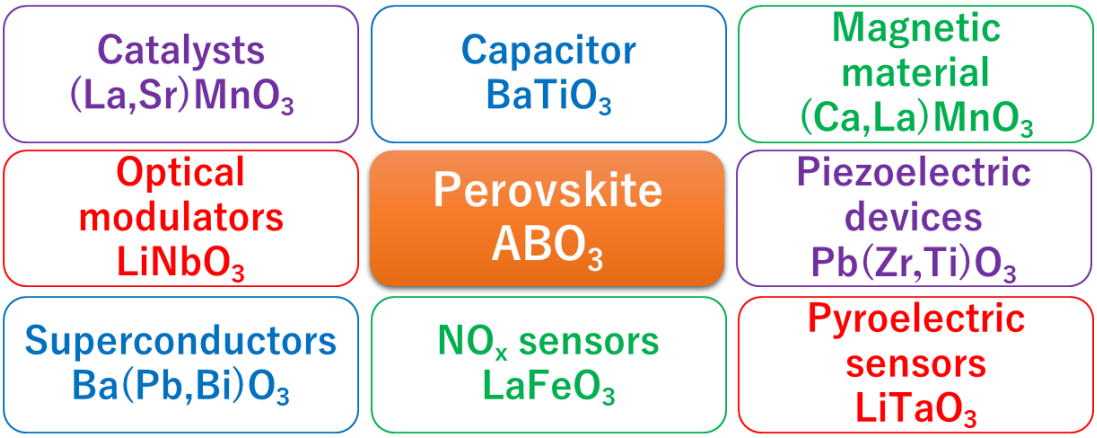

Fig. 1.3 Some examples of practically used perovskite-type oxides.

1.2. Control of properties by solid-solution formation

In the case of using perovskite-type oxides as functional materials, they are often formed into solid solutions by the addition of dopants to control and improve their original properties. The dopants either occupy interstitial sites or substitute for atoms or ions in the parent lattice. Two types of solid solutions are shown in Fig. 1.4. In substitutional solid solutions (Fig. 1.4(a)), introduced atom or ion directly replaces an atom or ion of the same charge in the parent structure. In interstitial solid solutions (Fig. 1.4(b)), introduced species occupies a site that is normally empty, and no ions or atoms are removed. The solid solutions of perovskite-type oxides are usually the substitutional solid solutions [1,26].

As an example of controlling physical property by forming solid solutions, $BaTiO_3$ case is given here. The dielectric property of $BaTiO_3$ is controlled by mixed with additives. As shown in Fig. 1.5, $BaTiO_3$ exhibits high permittivity around phase transition temperature, T_c = 120 °C [27]. In order to express this high permittivity at ambient temperature, two types of additives are used generally; T_c shifters and T_c depressors. The effect of the shifter and the depressor in the temperature dependence of permittivity is also drawn in Fig. 1.5 by blue and red broken lines. The shifters, such as $SrTiO_3$, $CaZrO_3$, $BaSnO_3$ and $PbTiO_3$, have the effect of shifting T_c to desired temperatures. The depressors, such as $CaTiO_3$, $MgZrO_3$ and $NiSnO_3$, as well as the shifters, are added to $BaTiO_3$ to depress the sharp change of the dielectric constant at around T_c for producing a flatter dielectric constant-temperature profile [28].

For a range of substitutional solid solutions to form, the ions that replace each other are required having the same charge and similar sizes in each other. For a solid solution to be stable, it must have lower free energy than that of a mere mixture of constituting materials. Free energy is composed of enthalpy and entropy terms, and this relation is shown as the following equation [1];

$$\Delta G = \Delta H - T\Delta S \qquad \text{eq. (1.1)}$$

Solid solutions always have larger entropy than the corresponding mere mixtures, because constituting ions are distributed at random in the atomic scale in their crystal structures. Thus the entropy term always favors solid-solution formation. On the other hand, the enthalpy term may or may not favor solid solutions to form depending on its sign. When the enthalpy change of a solid-solution formation is negative, constituting ions will dissolve and form a solid solution. If the enthalpy change is positive, then the enthalpy and entropy effect are opposed, and phase separation occurs. Such information is included in phase diagrams of the constituting materials, and phase diagrams represent temperature dependences of miscibility gaps [1,29].

There is a large amount of information about the solubility for perovskite-type oxide systems accumulated as phase diagrams, and the existence of solubility limits has been reported for many systems [30-34].

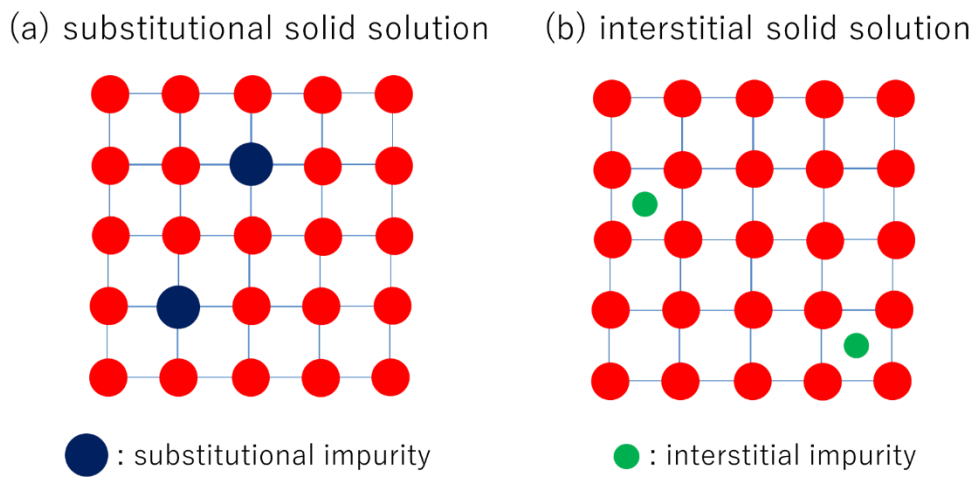

Fig. 1.4 Schematic drawing of solid solutions; (a) substitutional solid solution, (b) interstitial solid solution. Red circles express constituting ions and blue lines express unit cells, respectively.

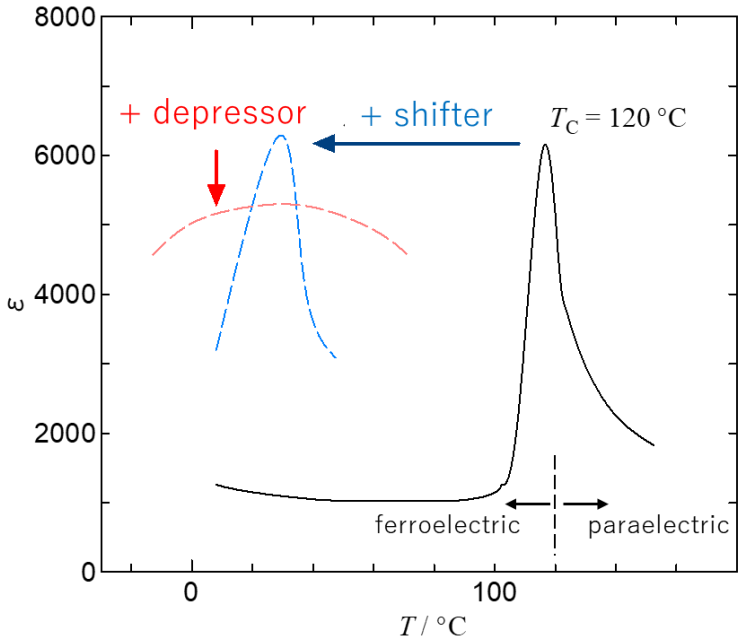

Fig. 1.5　Schematic drawing of the effect of shifter and depressor in the temperature dependence of permittivity for $BaTiO_3$.

1.3. Formation of amorphous film samples by sputtering

Schematic drawings of sputter apparatuses are shown in Fig. 1.6. The basic sputtering apparatus (Fig. 1.6(a)) contains a reduced pressure (10^{-1} to 10^{-2} torr) of inert gas, for example, argon. The gas is subjected to a potential drop in the order of kilovolt, creating a glow discharge from which positive ions are accelerated towards the target of the cathode. The produced high energy ions eject the material as sputtered clusters from the cathode, and the substrates are coated by the material of the target [1,35,36]. Sputtering is a surpassing method to obtain film samples which have greater adherence and uniformity [37]. However, there are some problems that are low deposition rate, low ionization efficiencies in the plasma, and so on [38].

Fig. 1.6(b) is a schematic drawing of the film sample formation in radio-frequency (rf) magnetron sputtering. Electrons are trapped around the target by the magnetic field there, and ionizing electron-atom collision increases in the sputtering chamber. Because of this, rf magnetron sputtering has a higher deposition rate with an increment of ionization efficiency [37,38] and can be used to form films from electrically insulating targets [39]. Rf magnetron sputtering is a valuable and efficient method to prepare film samples of oxides due to such advantages exceeding the basic sputtering method [37,38,40].

The sputtering of oxides is performed ordinarily with heating the substrates to obtain crystalline films. Without heating the substrates, amorphous film samples are formed usually because the sputtered clusters at high fictive temperatures are quenched on the substrates during depositions [41]. The formed amorphous film samples, in which

constituent ions disperse homogeneously, are expected to crystallize easily by annealing through short-range diffusions of the ions. Thus the sputtering and subsequent annealing have a high possibility of producing solid solutions in a wide composition range.

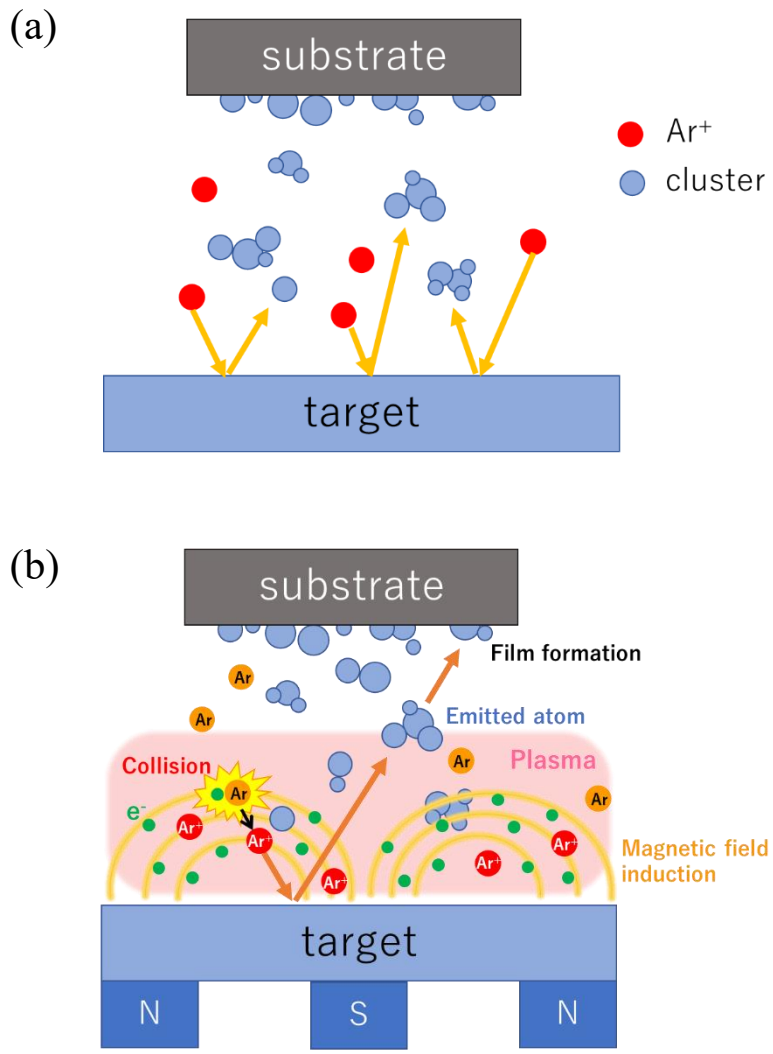

Fig. 1.6　Schematic drawing of film sample formation by sputtering (a), and that by rf magnetron sputtering (b).

1.4. Aim of this work

As mentioned above, amorphous film samples are potential materials to be converted to solid solutions by annealing without phase separation, and they can be formed by sputtering on to substrates at low temperatures. Despite the expected possibility of sputtering and subsequent annealing to produce solid solutions, sputtering of oxides is performed ordinarily with heating the substrates and such an approach to form solid solutions has never been examined so far to my knowledge.

Therefore, I tried to expand the solubility limit in perovskite-type oxide systems of $BaTiO_3$−$CaTiO_3$ and $BaZrO_3$−$CaZrO_3$ by applying the 'sputter-anneal' method, in which amorphous film samples were prepared by rf magnetron sputtering and annealed subsequently at a moderate temperature condition, with checking the formation of amorphous film samples and tracking the crystallization of the samples by annealing. I also investigated the composition dependence of the permittivity in the solid solutions of the systems.

References

[1] A. R. West, Basic Solid State Chemistry Second Edition, Wiley, Chichester, 1999, Chapters 1, 5 and 9.

[2] F. S. Galasso, STRUCTURE, PROPERTIES AND PREPARATION OF PEROVSKITE-TYPE COMPOUNDS, Pergamon Press, Oxford, 1969, Chapter 1.

[3] P. Ghosez, Microscopic Properties of Ferroelectric Oxides from First-Principles: Selected Topics (Troisieme Cycle de la Physique en Suisse Romande, Lausanne 2002). http://www.phythema.ulg.ac.be/Books

[4] R. J. D. Tilley, PEROVEKITES Structure Property Relationship, Kagaku-Dojin Publishing Company, INC, Tokyo, 2018, Chapters 1 and 6. [in Japanese]

[5] H. Megaw, Crystal Structures: A Working Apploach, Saunders, Philadelphia, 1973, pp. 285−304.

[6] B. G. Hyde, S. Andersson, Inorganic Crystal Structures, Wiley−Interscience, New York, 1989, pp. 295−304.

[7] O. Muller, R. Roy, The Major Ternary Structural Families, Springer−Verlag, Berlin, 1974, pp. 175−196.

[8] V. V. M. Goldschmidt, Die Gesetze der Krystallochemie, M. Naturwissenschaften 14 (1926) 477. https://doi.org/10.1007/BF01507527

[9] A. S. Bhalla, R. Guo, R. Roy, The perovskite structure – a review of its role in ceramic science and technology, Mat. Res. Inovat. 4 (2000) 3−26. https://doi.org/10.1007/s100190000062

[10] R. Roy, Multiple Ion Substitution in the Perovskite Lattice, J. Am. Ceram. Soc. 37 (1954) 581−588. https://doi.org/10.1111/j.1151-2916.1954.tb13992.x

[11] M. Lorenz *et al*., The 2016 oxide electronic materials and oxide interfaces roadmap, J. Phys. D: Appl. Phys. 49 (2016) 433001. https://doi.org/10.1088/0022-3727/49/43/433001

[12] X. M. Chen, T. Wang, J. Li, Dielectric characteristics and their field dependence of (Ba,Ca)TiO_3 ceramics, Mater. Sci. Eng. B 113 (2004) 117−120. https://doi.org/10.1016/j.mseb.2004.04.003

[13] S. -H. Yao, J. -K. Yuan, P. Gonon, J. Bai, S. Pairis, A. Sylvestre, Effect of oxygen vacancy on the dielectric relaxation of $BaTiO_3$ thin films in a quenched state, J. Appl. Phys. 111 (2012) 104109. https://doi.org/10.1063/1.4717758

[14] D. Fu, M. Itoh, S. Koshihara, Invariant lattice strain and polarization in $BaTiO_3$–$CaTiO_3$ ferroelectric alloys, J. Phys.: Condens. Matter 22 (2010) 052204. https://doi.org/10.1088/0953-8984/22/5/052204

[15] D. Fu and M. Itoh, Role of Ca off-centering in tuning the ferroelectric phase transitions in Ba(Zr,Ti)O_3 system, 2015. arXiv:1503.00406 [cond-mat.mtrl-sci]

[16] X. N. Zhu, T. T. Gao, X. Xu, W. Z. Liang, Y. Lin, C. Chen, X. M. Chen, Piezoelectric and Dielectric Properties of Multilayered $BaTiO_3$/(Ba,Ca)TiO_3/$CaTiO_3$ Thin Films, ACS Appl. Mater. Interfaces 8 (2016) 22309−22315. https://doi.org/10.1021/acsami.6b05469

[17] N. Wang, D. Kong, H. He, Solvothermal synthesis of strontium titanate nanocrystallines from metatitanic acid and photocatalytic activities, Powder Tech. 207 (2011) 470−473. https://doi.org/10.1016/j.powtec.2010.11.034

[18] L. F. Silva, O. F. Lopes, V. R. Mendonca, K. T. G. Carvalho, E. Longo, C. Ribeiro, V. R. Mastelaro, An Understanding of the Photocatalytic Properties and Pollutant Degradation Mechanism of $SrTiO_3$ Nanoparticles, Photochemistry and Photobiology,

92 (2016) 371−378. https://doi.org/10.1111/php.12586

[19] G. Wu, P. Li, D. Xu, B. Luo, Y. Hong, W. Shi, C. Liu, Hydrothermal synthesis and visible-light-driven photocatalytic degradation for tetracycline of Mn−doped $SrTiO_3$ nanocubes, Appl. Surf. Sci. 333 (2015) 39−47. https://doi.org/10.1016/j.apsusc.2015.02.008

[20] N. Mahato, A. Banerjee, A. Gupta, S. Omar, K. Balani, Progress in material selection for solid oxide fuel cell technology: A review, Prog. Mater. Sci. 72 (2015) 141−337. https://doi.org/10.1016/j.pmatsci.2015.01.001

[21] A. M. Abdalla, S. Hossain, A. T. Azad, P. M. I, Petra, F. Begum, S. G. Eriksson, A. K. Azad, Nanomaterials for solid oxide fuel cells: A review, Renew. Sust. Energ. Rev. 82 (2018) 353−368. https://doi.org/10.1016/j.rser.2017.09.046

[22] P. Kanhere, Z. Chen, A Review on Visible Light Active Perovskite-Based Photocatalysts, Molecules 19 (2014) 19995−20022. https://doi.org/10.3390/molecules191219995

[23] S. Keav, S. K. Matam, D. Ferri, A. Weidenkaff, Structured Perovskite−Based Catalysts and Their Application as Three-Way Catalytic Converters−A Review, Catalysts 4 (2014) 226−255. https://doi.org/10.3390/catal4030226

[24] A. Chroneos, R. V. Vovk, I. L. Goulatis, L. I. Goulatis, Oxygen transport in perovskite and related oxides: A brief review, J. Alloy. Compd. 494 (2010) 190−195. https://doi.org/10.1016/j.jallcom.2010.01.071

[25] The Ceramic Society of Japan, Advanced Ceramic Technologies & Products, Springer, Tokyo, 2012.

[26] R. D. Tilley, UNDERSTANDING SOLIDS The Science of Materials Second Edition, Wiley, 2013.

[27] R. C. Ropp, Encyclopedia of the Alkaline Earth Compounds, Elsevier, Amsterdam, 2013, p. 671.

[28] G. H. Heartling. Ferroelectric Ceramics: History and Technology, J. Am. Ceram. Soc. 4 (1999) 797−818. https://doi.org/10.1111/j.1151-2916.1999.tb01840.x

[29] C. Kittel, Introduction to Solid State Physics EIGHTH EDITION, John Wiley & Sons, Inc, USA, 2005, Chapter 22.

[30] M. McQuarrie, Structural Behavior in the System (Ba, Ca, Sr)TiO_3 and Its Relation to Certain Dielectric Characteristics, J. Am. Ceram. Soc. 38 (1955) 444–449. https://doi.org/10.1111/j.1151-2916.1955.tb14571.x

[31] R. C. DeVries, R. Roy, Phase Equilibria in the System $BaTiO_3$-$CaTiO_3$, J. Am. Ceram. Soc. 38 (1955) 142–146. https://doi.org/10.1111/j.1151-2916.1955.tb14918.x

[32] I. Levin, T. G. Amos, S. M. Bell, L. Farber, T. A. Vanderah, R. S. Roth, B. H. Toby, Phase equilibria, crystal structures, and dielectric anomaly in the $BaZrO_3$-$CaZrO_3$ system, J. Solid State Chem. 175 (2003) 170–181. https://doi.org/10.1016/S0022-4596(03)00220-2

[33] H. Yang, K. Kan, J. Ouyang, Y. Li, Solvothermal synthesis and optical properties of Mn^{2+}-doped $SrTiO_3$ powders, J. Alloy. Compd. 485 (2009) 351−355. https://doi.org/10.1016/j.jallcom.2009.05.109

[34] E. M. Levin, Phase diagrams for ceramists, American Ceramic Society, Ohio, 1975.

[35] D. L. Smith, Thin-Film Deposition Principles and Practice, McGraw-Hill, Inc., Boston, 1995, Chapter 9.

[36] M. Qadir, Y. Li, C. Wen, Ion-substituted calcium phosphate coatings by physical vapor deposition magnetron sputtering for biomedical applications: A review, Acta Biomaterialia 89 (2019) 14−32. https://doi.org/10.1016/j.actbio.2019.03.006

[37] K. J. Klabunde, Thin Films from Free Atoms and Particles, ACADEMIC PRESS, INC, Orlando, 1985, pp. 257–258.

[38] P. J. Kelly, R.D. Arnell, Magnetron sputtering: a review of recent developments and applications, Vacuum 56 (2000) 159−172. https://doi.org/10.1016/S0042-207X(99)00189-X

[39] J. E. Mahan, PHYSICAL VAPOR DEPOSITION OF THIN FILMS, JOHN WILEY & SONS, INC., New York, 2000, pp. 156–157.

[40] R. V. Stuart, Vacuum Technology, Thin Films, and Sputtering An Introduction, ACADEMIC PRESS, INC., London, 1983, pp. 130–131.

[41] P. Gonon, F. E. Kamel, Dielectric response of Cu/amorphous $BaTiO_3$/Cu capacitors, J. Appl. Phys. 101 (2007) 073901. https://doi.org/10.1063/1.2716871

Chapter 2. Formation of $Ba_{1-x}Ca_xTiO_3$ solid solutions without miscibility gap and their dielectric properties

Abstract

To produce $Ba_{1-x}Ca_xTiO_3$ solid solutions beyond the solubility limit, I performed rf magnetron sputtering using the targets of $(BaTiO_3)_{1-x}(CaTiO_3)_x$ with compositions x from 0 to 1 onto quartz glass substrates without heating the substrates and annealed the formed film samples. The as-prepared film samples by the sputtering were confirmed to have amorphous structures. By annealing the as-prepared amorphous film samples at the rather low temperature of 800 °C for 3 h, crystallization proceeded in the samples, and I successfully obtained $Ba_{1-x}Ca_xTiO_3$ solid solutions in whole the composition range without phase separation. The permittivity of the formed solid solutions exhibited a peculiar Ca composition dependence. The dependence was well explained by the formation of extra space around Ca^{2+} ions substituted for Ba^{2+} ions.

2.1. Introduction

Barium titanate ($BaTiO_3$) is an important dielectric material possessing ferroelectric, piezoelectric and pyroelectric properties at room temperature, and used for capacitors, piezoelectric devices, and so on [1-4]. In actual applications, $BaTiO_3$ is combined with additives such as calcium titanate ($CaTiO_3$) to control its functional properties, and $Ba_{1-x}Ca_xTiO_3$ solid solutions have received considerable attention as lead-free materials among the modified $BaTiO_3$-based materials [5,6]. The formation methods and properties of $Ba_{1-x}Ca_xTiO_3$ solid solutions have been investigated widely [7-13], and solubility limits have been reported to be $x \leq 0.23$ and $0.87 \leq x$ in the conventional solid-state reaction [9,10] and $x \leq 0.34$ in the floating zone method [11]. The $Ba_{1-x}Ca_xTiO_3$ solid solutions with the compositions close to the solubility limit exhibit interesting properties such as high permittivity at low temperatures, small temperature coefficient of permittivity and large electrostriction [14-16]. The extension of the solubility limit would make possible the investigation about the origin of those properties and also open new applications of $Ba_{1-x}Ca_xTiO_3$ as functional materials [17,18].

Rf magnetron sputtering is a valuable and efficient method to prepare film samples of oxides [19], and, without heating the substrates, amorphous film samples are formed usually because the sputtered clusters at high fictive temperatures are quenched on the substrates during depositions [20]. The formed amorphous film samples, in which constituent ions disperse homogeneously, are expected to crystallize easily by annealing through short-range diffusions of the ions. Thus the sputtering and successive annealing have a high possibility of producing solid solutions in wide composition range. However,

the sputtering of oxides is performed ordinarily with heating the substrates and such an approach to form solid solutions has never been examined so far to my knowledge.

Therefore, I tried to expand the solubility limit in $Ba_{1-x}Ca_xTiO_3$ system by applying the 'sputter-anneal' method with checking the formation of amorphous film samples and tracking the crystallization of the samples by annealing. The method was found to work effectively, and $Ba_{1-x}Ca_xTiO_3$ solid-solution film samples were formed successfully in whole the composition range of $0 \leq x \leq 1$. I also investigated Ca composition dependence of the permittivity in $Ba_{1-x}Ca_xTiO_3$ solid-solution film samples prepared by the method.

2.2. Experimental section

$(BaTiO_3)_{1-x}(CaTiO_3)_x$ powder samples with compositions of x = 0, 0.20, 0.35, 0.50, 0.70, 0.90 and 1 were prepared by calcining raw materials of $BaCO_3$, $CaCO_3$ and TiO_2 weighed to the desired compositions at 1000 °C for 12 h. The powder samples were pressed into disks and sintered at 1400 °C for 6 h. Then the formed disks were polished and shaped into targets for sputtering with a diameter of 1 inch and 2 mm thick. The details of the samples used are given in Table 2.1, and the photograph of a typical sample of the sintered disks and that of the targets set to the holder for sputtering are shown in Fig. 2.1. The densities and sintering degree of the prepared targets are listed in Table 2.2.

With using the disk-shaped $(BaTiO_3)_{1-x}(CaTiO_3)_x$ targets, film samples were formed on quartz glass substrates (10 mm × 10 mm × 0.8 mm*t*) by a conventional upward type rf magnetron sputtering apparatus (ULVAC, SCOTT-C3-T1). The sputtering was performed under Ar (1.0 Pa) / O_2 (0.4 Pa) mixed gas atmosphere with rf power of 30 W. The substrate was mounted 40 mm above the target, and sputtering time was set from 4.5 to 12 h for each target separately to control the thickness of the film samples to be ~1 μm. The thicknesses of the film samples formed were estimated to be 900–1300 nm by using a laser scanning microscope (Olympus, LEXT OLS4000). Annealing of the film samples was performed by using an electric furnace under atmospheric condition. The heating rate was set to be 200 °C h^{-1}, and the samples were kept at the desired temperature for 3 h.

X-ray diffraction (XRD) experiments were carried out with a powder X-ray diffractometer (Rigaku, RINT 2200VF) by using Cu Kα radiation. Diffraction angles were calibrated by using a reference Si sample as an external standard. Measurement

conditions in the XRD are listed in Table 2.3. Grain sizes D of crystalline samples were estimated from the width of diffraction peaks by using Scherrer equation [21-23]:

$$D = \frac{\mathrm{K}\lambda}{B\cos\theta} \qquad \text{eq. (2.1)}$$

$$B = \sqrt{B_{\mathrm{obs}} - B_{\mathrm{inst}}} \qquad \text{eq. (2.2)}$$

here, K is shape factor and usually in the range $0.89 - 0.91$, λ is the wavelength of X-ray, B is a corrected line breadth at half the maximum intensity in radians after subtracting the instrumental line broadening, and θ is the Bragg angle. In this study, K = 0.90 and λ = 1.54×10^{-10} m were used in the equation.

For dielectric measurements, $Ba_{1-x}Ca_xTiO_3$ film samples were formed on Nb(1.0 wt%)-doped $SrTiO_3$ single crystals purchased from Furuuchi Chemical ($SrTiO_3$:Nb; 10 mm × 10 mm × 0.5 mm*t* with (100) polished plane), which have electric conductivity of ~400 S cm^{-1}, by the sputtering in the same manner as onto the quartz glass substrate. Pt electrode (1.7×1.7 mm^2) was prepared on the surface of each sample by the sputtering under Ar (~2 Pa) atmosphere as the upper electrode. In the annealed samples, Pt-electrode preparation was performed after the annealing. The schematic view of the sample at electric measurements and the cross-section drawing of the sample are shown in Fig. 2.2(a) and (b), respectively. The measurements were carried out by using a Sawyer-Tower circuit [24] (Fig. 2.3) by applying the oscillating electric field in the frequency of 1 kHz with the magnitude of 500 mV_{rms} between the $SrTiO_3$:Nb substrate and the Pt electrode.

Dielectric measurements were also performed by using an impedance analyzer (Solartron, SI1260) equipped with an electrochemical interface (Solartron, SI1287) in the frequency range $1–10^5$ Hz by applying the oscillating electric field of 10 mV_{rms} between the $SrTiO_3$:Nb substrate and the Pt electrode. The obtained data were analyzed according to complex admittance Y^* formalism.

Table 2.1 List of chemicals used, their source and purity

Chemicals	Source	Purity	Analysis method
$BaCO_3$	Wako Pure Chemical Industries	0.999[a]	Manufacturer assay
$CaCO_3$	Kanto Kagaku	0.9999[a]	Manufacturer assay
TiO_2 (anatase)	Rare Metallic	0.9999[a]	Manufacturer assay
$(BaTiO_3)_{1-x}(CaTiO_3)_x$; x = 0, 0.20, 0.35, 0.50, 0.70, 0.90 and 1	Synthesized in this study	0.99[b]	XRD[c]
Argon	Kansan Corporation	0.9999[a]	Manufacturer assay
Oxygen	Kansan Corporation	0.995[a]	Manufacturer assay
Platinum	Furuya Metal Co., Ltd.	0.999[a]	Manufacturer assay

[a] Mass fraction purity.

[b] The lowest estimation of mole fraction purity.

[c] X-ray diffractometry (Fig. 2.4).

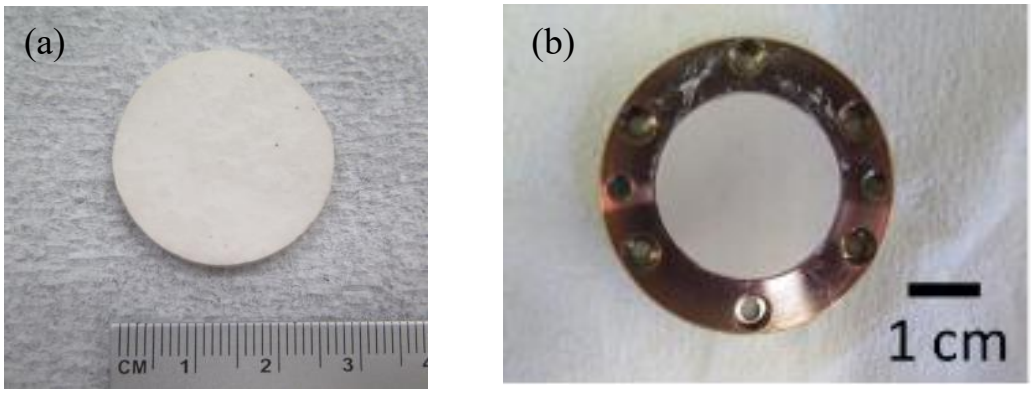

Fig. 2.1　Photograph of a typical sample of the sintered disks (a), and that of the targets set to the holder of the sputtering apparatus (b).

Table 2.2 Densities and sintering degrees of the $Ba_{1-x}Ca_xTiO_3$ targets

Ca composition x	Theoretical density (g cm^{-3})	Density (g cm^{-3})	Sintering degree (%)
0	6.01	3.62	60.2
0.20	5.62	4.93	87.6
0.35	5.32	2.88	57.7
0.50	5.02	4.54	90.4
0.70	4.62	2.58	55.8
0.90	4.23	2.38	56.3
1	4.03	3.08	76.4

Table 2.3 Measurement conditions in XRD experiments

Measuring method	Continuous mode	Fixed time mode
Scanning axis	θ / 2θ	θ / 2θ
Initial angle (°)	10.000	10.000
Final angle (°)	80.000	80.000
Sampling width (°)	0.02	0.010
Scanning speed (°/ min)	4.000	–
Gate time (sec)	–	1.0
X-ray tube voltage (kV)	40	40
X-ray tube current (mA)	20	20

(a)

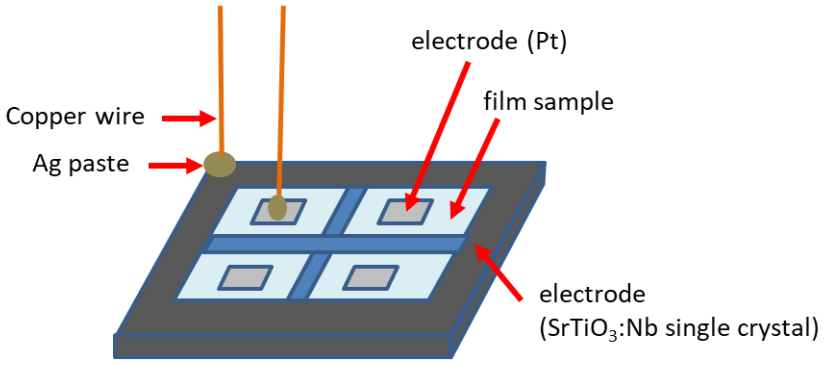

(b)

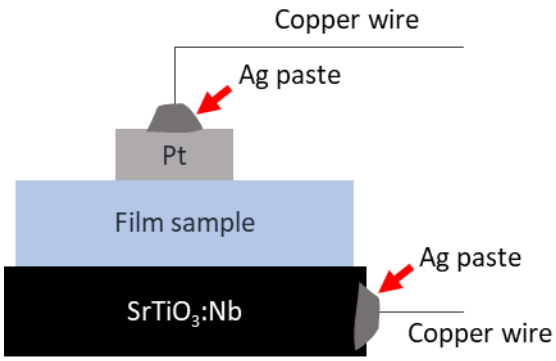

Fig. 2.2 Schematic view of the sample at electric measurements (a), and the cross-section drawing of the sample (b).

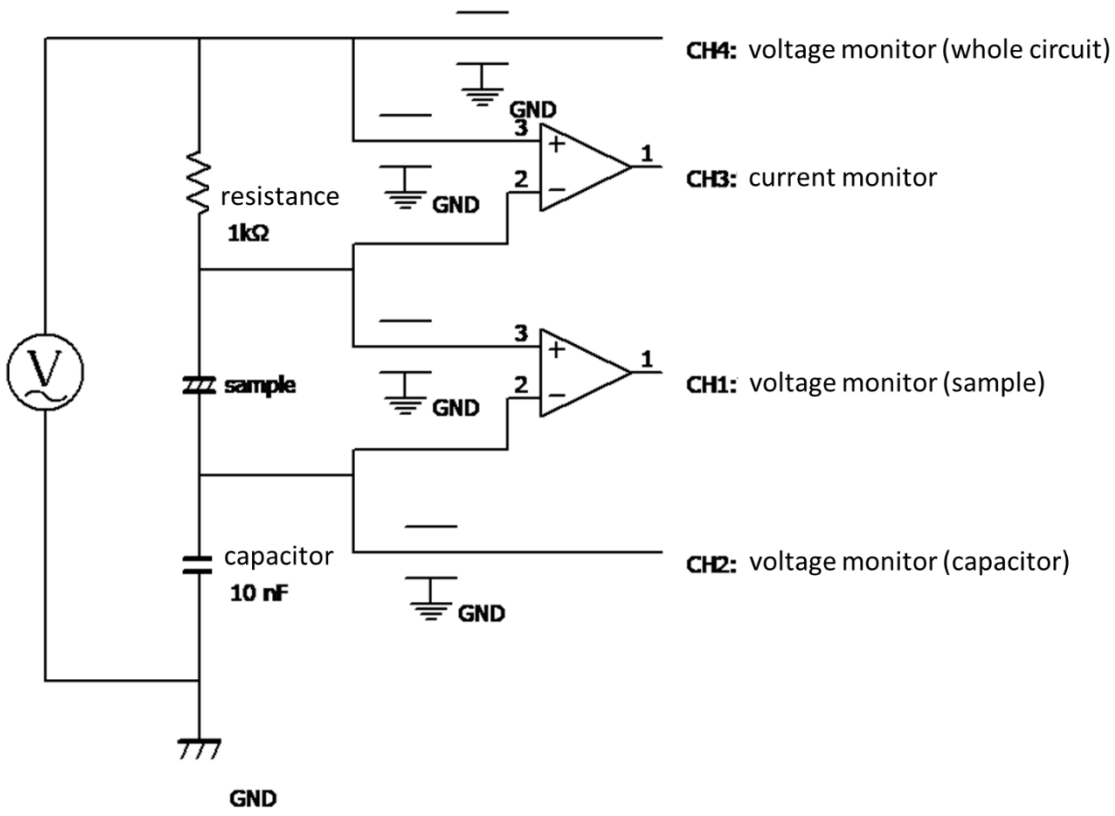

Fig. 2.3 Schematic diagram of the Sawyer-Tower circuit used in this study.

2.3. Results and discussions

2.3.1. Formation of $Ba_{1-x}Ca_xTiO_3$ solid solutions

Fig. 2.4(a) shows the results of the XRD experiments for $Ba_{1-x}Ca_xTiO_3$ targets used in the sputtering along with the XRD patterns of $BaTiO_3$ (ICDD No 00-005-0626) and $CaTiO_3$ (ICDD No 01-076-2400). The $x = 0$ ($BaTiO_3$) and $x = 1$ ($CaTiO_3$) targets gave the diffraction patterns well corresponding to those reported for $BaTiO_3$ and $CaTiO_3$, respectively. Fig. 2.4(b) is the enlarged view of the diffractions of the targets. The targets with the Ca compositions $x = 0.35$, 0.50 and 0.70 exhibited the patterns by the coexistence of Ba-rich and Ca-rich phases as the indication of the phase separation occurred in the preparation process, the calcination and the sintering, of the targets.

Fig. 2.5(a) is a photograph of a typical sample of the as-prepared films deposited on the quartz glass substrates by the sputtering using the $(BaTiO_3)_{0.50}(CaTiO_3)_{0.50}$ target, and Fig. 2.5(b) is a surface image and roughness profile of the as-prepared film sample observed by the laser scanning microscope. As shown in Fig. 2.5(b), the surface of the film sample is rather flat and smooth. XRD patterns of the as-prepared film samples are shown in Fig. 2.6. All the samples exhibited broadened halo patterns characteristic of amorphous structures at around $2\theta = 30°$ overlapped with the diffraction due to the quartz glass substrate. To obtain the information about crystallization of the amorphous film samples by annealing, I attempted annealing the as-prepared $BaTiO_3$ film samples at the temperatures from 400 to 1000 °C for 3 h. The XRD patterns of the annealed samples are shown in Fig. 2.7 with that of $BaTiO_3$ powder sample. The patterns of tetragonal and

cubic $BaTiO_3$ (ICDD No 00-066-0196) are also shown in the figure. Diffraction peaks of crystalline $BaTiO_3$ started to appear by the annealing at a rather low temperature of 500 °C, as expected in the amorphous sample. The diffraction patterns of the annealed samples are well correspondent to that of $BaTiO_3$ in a cubic structure, indicating that the formed crystallites have the cubic structure. As shown in Fig. 2.8, the area intensity of the diffraction peak corresponding to 111 plane increased with the rise of the annealing temperature up to 800 °C, then decreased slightly by the annealing at 900 °C although the peaks became sharper by the crystal growth, and the formation of byproducts was observed by the annealing at 1000 °C. The sample annealed at 800 °C exhibited broader diffraction peaks than those of the powder sample, which can originate in the smallness of the grain size of the formed crystallites, and the grain size was estimated to be ~50 nm from the width of the diffraction peak of 111 by using Scherrer equation [23].

In Fig. 2.9, the diffraction peak at around $2\theta = 56°$ of the annealed film sample is shown with those of $BaTiO_3$ powder sample. The powder sample exhibited two separate peaks due to (112) and (211) planes based on its tetragonal crystalline structure, and each peak was split into the diffractions by Cu $K\alpha_1$ and $K\alpha_2$ lines (Fig. 2.9 (a)). By assuming the grain size of 50 nm, the diffraction peaks of the powder sample are broadened and re-composed into a diffraction peak shown in Fig. 2.9 (b). The simulated peak exhibits no clear splitting but still has a shoulder in the lower angle side due to the separation of the diffractions by (112) and (211) planes. Differently from the simulated peak, the annealed sample showed only one broadened peak with a rather symmetric shape (Fig. 2.9 (c)). From this comparison, the annealed film sample is concluded to consist of crystallites having cubic structure, possibly due to the smallness of the grain size.

Based on the results of the annealing in the as-prepared $BaTiO_3$ amorphous film samples, I applied the annealing at 800 °C for 3 h to other amorphous film samples formed by the sputtering with using the $(BaTiO_3)_{1-x}(CaTiO_3)_x$ targets. Fig. 2.10 shows the XRD patterns of the annealed film samples along with the patterns of tetragonal $BaTiO_3$, cubic $BaTiO_3$ and orthorhombic $CaTiO_3$. All the annealed samples exhibited diffraction peaks, as in the case of the $BaTiO_3$ film sample, indicating that the crystallization proceeded in all the amorphous film samples at the rather low temperature of 800 °C. Fig. 2.11(a) is a photograph of the annealed film sample formed on the quartz glass substrate by the sputtering with using the $(BaTiO_3)_{0.50}(CaTiO_3)_{0.50}$ target, and Fig. 2.11(b) is a surface image and roughness profile of the annealed film sample observed by the laser scanning microscope. Mechanical cracks were generated in the annealed sample on the quartz glass substrate, probably due to the mismatch of thermal expansion coefficients between the film samples and the substrate [25,26]. Additional annealing at 800 °C for 12 h in the x = 0.50 sample did not affect the area intensity of the diffraction peaks nor the diffraction pattern, and thus the crystallization of the samples by the annealing at 800 °C are considered to complete within 3 h as shown in Fig. 2.12.

The enlarged view of the diffractions of the annealed samples in the range of 2θ from 54° to 61° is shown in Fig. 2.13. The diffraction peak of each sample indexed as 112 and 211 of tetragonal $BaTiO_3$ or 123, 042 and 240 of orthorhombic $CaTiO_3$ was observed as a single peak without splitting. The results exhibit that no phase separation occurred in the samples during the crystallization and that the formed crystallites have cubic structures.

As seen in Fig. 2.10 and 2.13, the positions of the diffraction peaks shifted to higher angles continuously with the Ca composition x of the target, and the shift was

considered to be produced by the substitution of the Ba^{2+} ions by the smaller Ca^{2+} ions [27]. To analyze the structural change of the crystalline film samples with the Ca composition, I evaluated the lattice constants of the samples from the angles of the diffraction peaks due to (110), (200) and (211) planes in cubic structure by using Cell Calc [28]. The estimated lattice constants *a* are plotted as the function of the Ca composition *x* of the target in Fig. 2.14 and listed in Table 2.5. A continuous and linear relation was observed between *x* and *a*. The continuity and the fact that no phase separation was observed in the samples evidence the formation of monophasic $Ba_{1-x}Ca_xTiO_3$ solid solutions in whole the Ca composition range, and the linear relation shows that the formed crystalline film samples have the same compositions, respectively, of the targets used for the sputtering according to Vegard's law [29].

In the syntheses of $Ba_{1-x}Ca_xTiO_3$ by a conventional solid-state reaction method, samples are kept at higher temperatures than 1200 °C usually, and in the case of a floating zone method, raw materials are melted at much higher temperatures to form single crystals. Such high-temperature treatments cause long-range diffusions of the constituent ions in the $Ba_{1-x}Ca_xTiO_3$ samples with producing phase separations at the compositions out of the solubility limit (Fig. 2.15 (a)). In this study, on the other hand, the amorphous $Ba_{1-x}Ca_xTiO_3$ film samples were formed by the sputtering, and the samples were annealed at the rather low temperature of 800 °C. At the temperature, only short-range diffusions are allowed to the ions constituting the samples, and such limited diffusions cannot cause phase separations. However, the short-range diffusions of the ions are enough for the amorphous samples to crystallize into solid solutions since the constituent ions disperse homogeneously and continuously without grain boundaries in the amorphous samples (Fig. 2.15 (b)). In other words, the amorphous film sample has the structure at a high

fictive temperature, and thus the solid solution was formed as a meta-stable phase by the annealing at the moderate condition. The solid solutions of $Ba_{1-x}Ca_xTiO_3$, especially in the Ca composition range beyond the solubility limit reported so far for the system, i.e., x = 0.35, 0.50 and 0.70, are considered to be formed by the present 'sputter-anneal' method in the manner without phase separations.

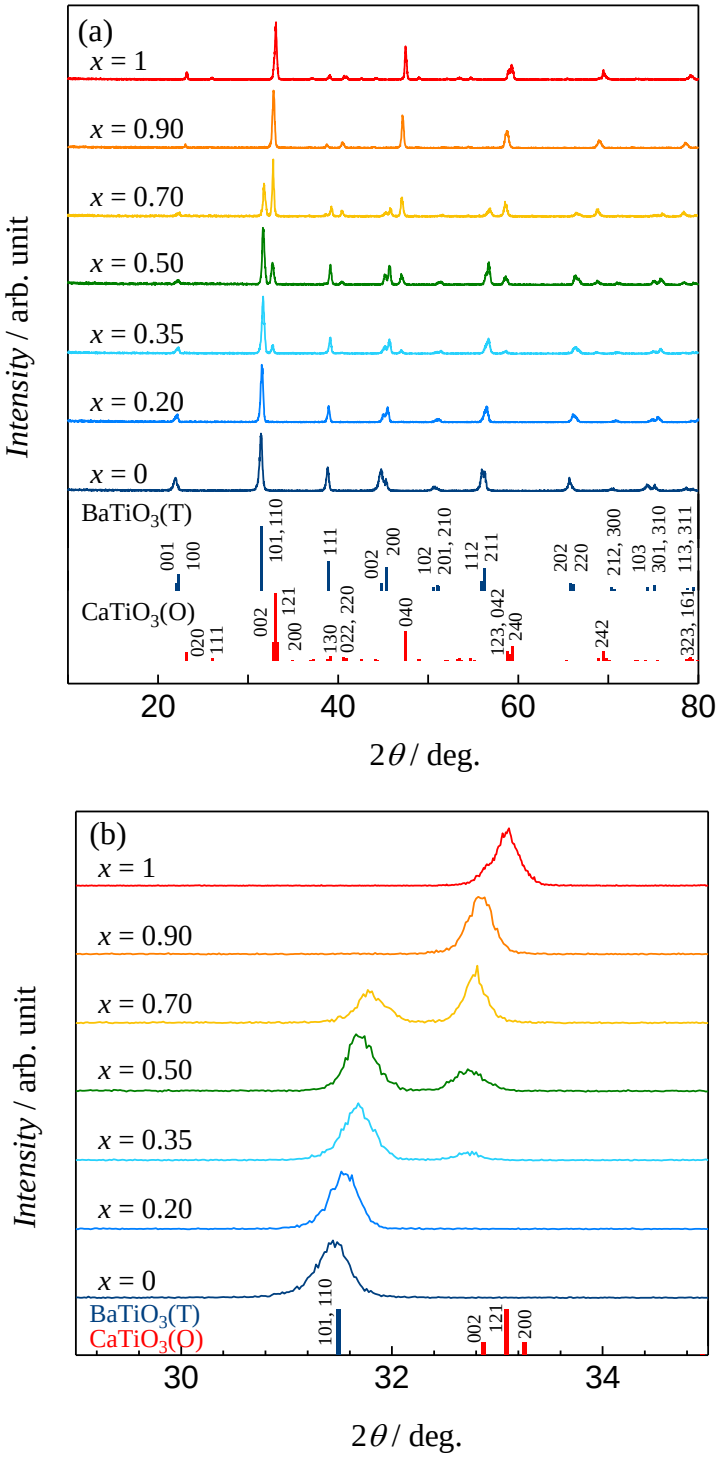

Fig. 2.4 XRD patterns of the $Ba_{1-x}Ca_xTiO_3$ targets (a), and the enlarged view of the patterns (b).

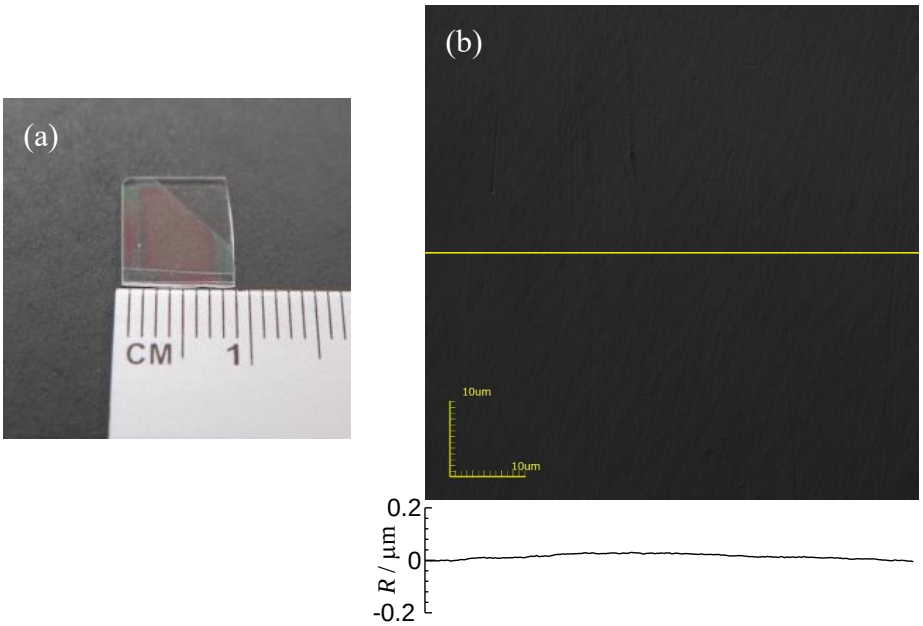

Fig. 2.5 As-prepared film sample deposited on the quartz glass substrate by the sputtering with using the $(BaTiO_3)_{0.50}(CaTiO_3)_{0.50}$ target; (a) photograph of the sample, (b) surface image and roughness profile observed by laser scanning microscope. Surface roughness, *R*, was measured along the yellow line indicated in the image.

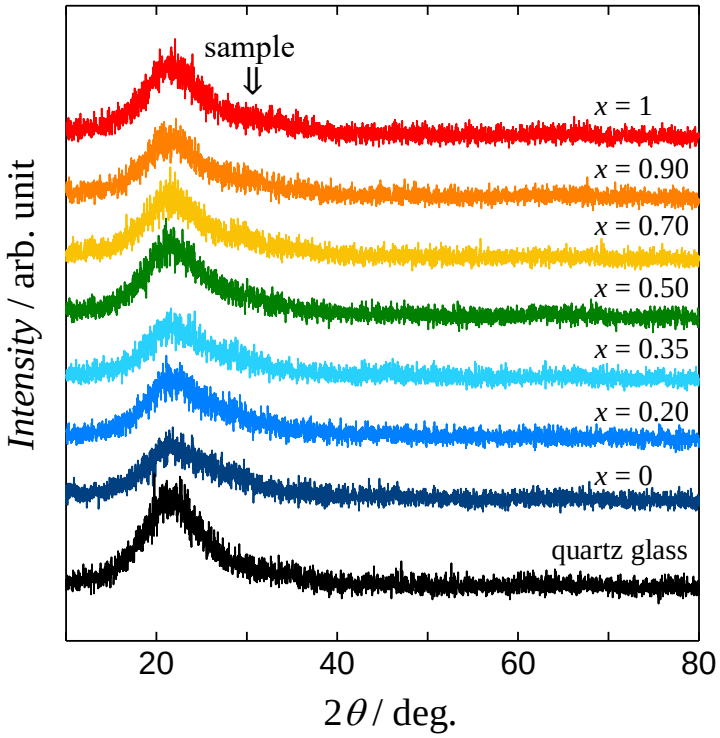

Fig. 2.6 XRD patterns of the as-prepared film samples formed by the rf magnetron sputtering with using the $(BaTiO_3)_{1-x}(CaTiO_3)_x$ targets and that of the quartz glass substrate.

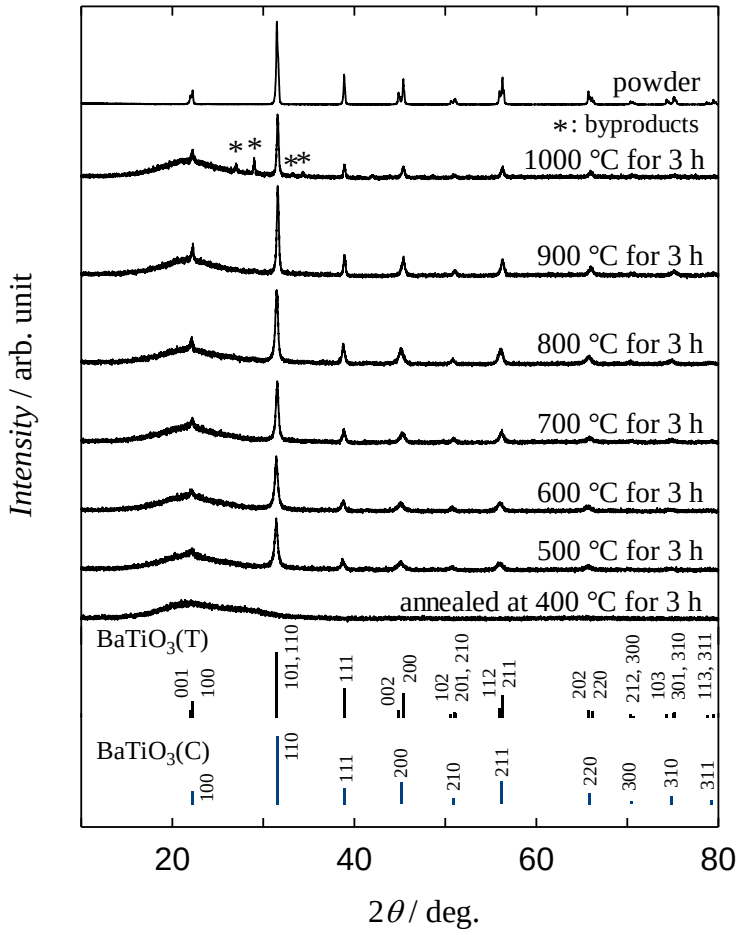

Fig. 2.7 XRD patterns of the annealed $BaTiO_3$ film samples and powder sample of $BaTiO_3$. The lines at the bottom represent the diffraction patterns of tetragonal and cubic $BaTiO_3$.

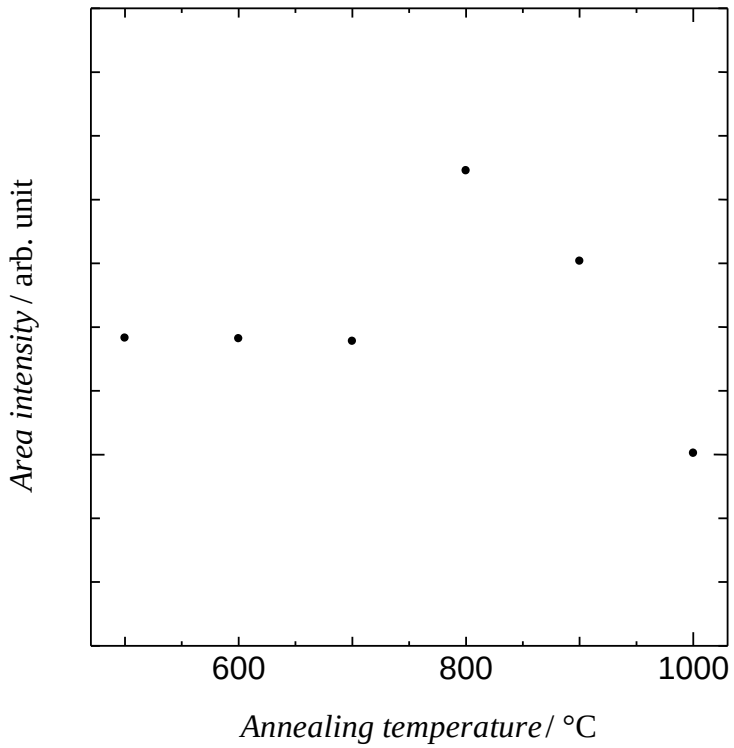

Fig. 2.8 The area intensity of the diffraction peak corresponding to 111 plane in annealed $BaTiO_3$ samples.

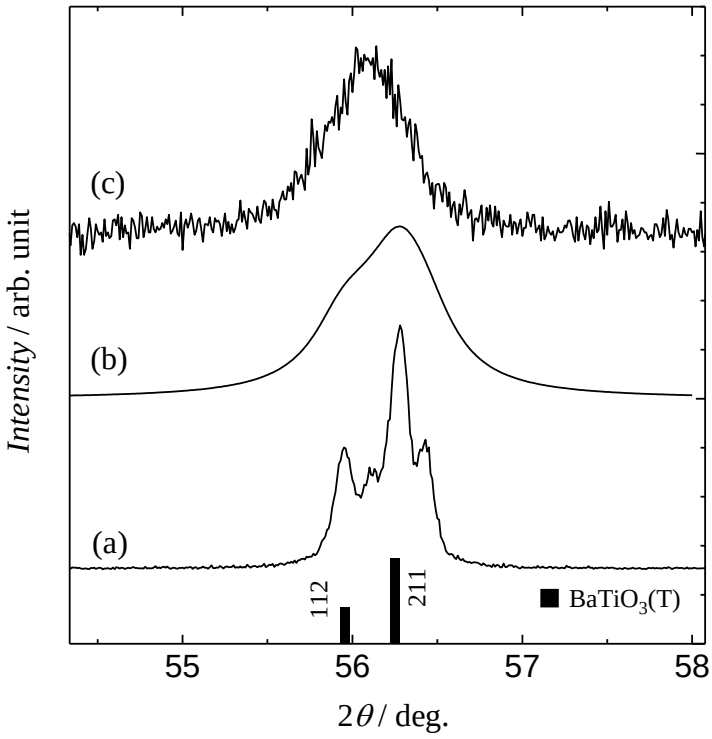

Fig. 2.9 XRD diffraction peaks of $BaTiO_3$ at around $2\theta = 56°$; (a) powder sample, (b) simulated with assuming the crystalline grain size D = 50 nm, and (c) annealed film sample. The lines at the bottom represent the diffraction pattern of tetragonal $BaTiO_3$.

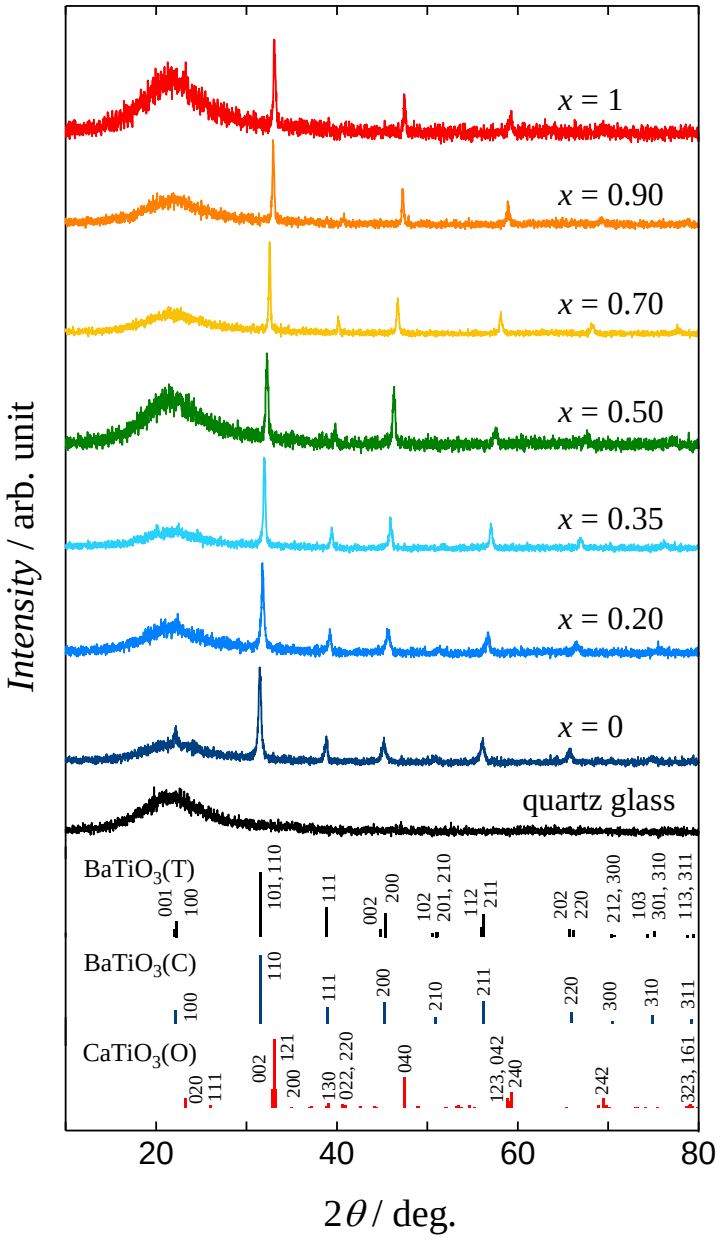

Fig. 2.10 XRD patterns of the annealed film samples formed by the sputtering with using the $(BaTiO_3)_{1-x}(CaTiO_3)_x$ targets and that of the quartz glass plate used as the substrate. The lines at the bottom represent the diffraction patterns of tetragonal $BaTiO_3$, cubic $BaTiO_3$ and orthorhombic $CaTiO_3$.

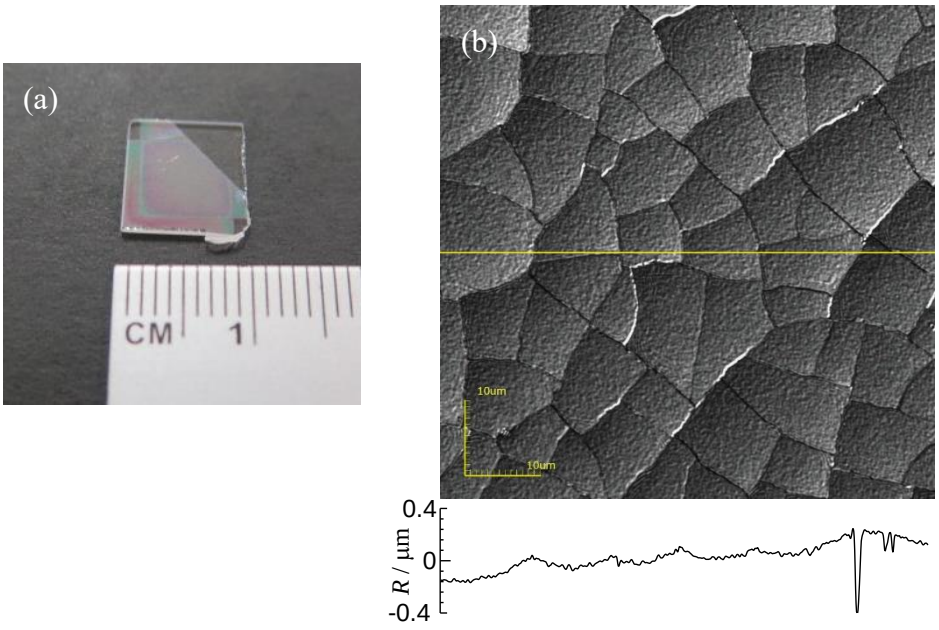

Fig. 2.11 Annealed film sample formed on the quartz glass substrate by the sputtering with using the $(BaTiO_3)_{0.50}(CaTiO_3)_{0.50}$ target; (a) photograph of the sample, (b) surface image and roughness profile observed by laser scanning microscope. Surface roughness, *R*, was measured along the yellow line indicated in the image.

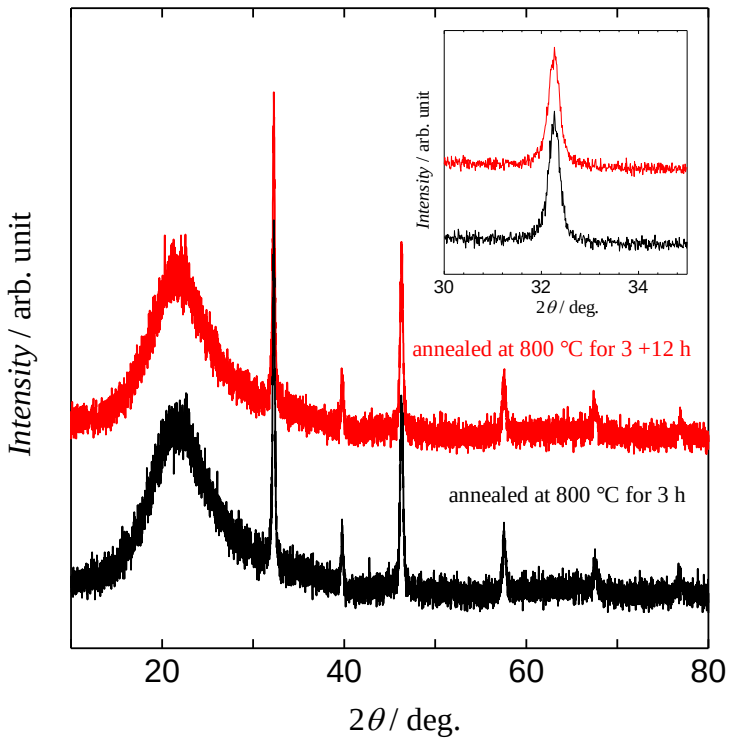

Fig. 2.12　XRD pattern of $Ba_{0.50}Ca_{0.50}TiO_3$ film sample annealed at 800 °C for 3 h (black line) and that after additional annealing for 12 h (red line). Inset is an enlarged view of the diffractions around $2\theta = 32°$.

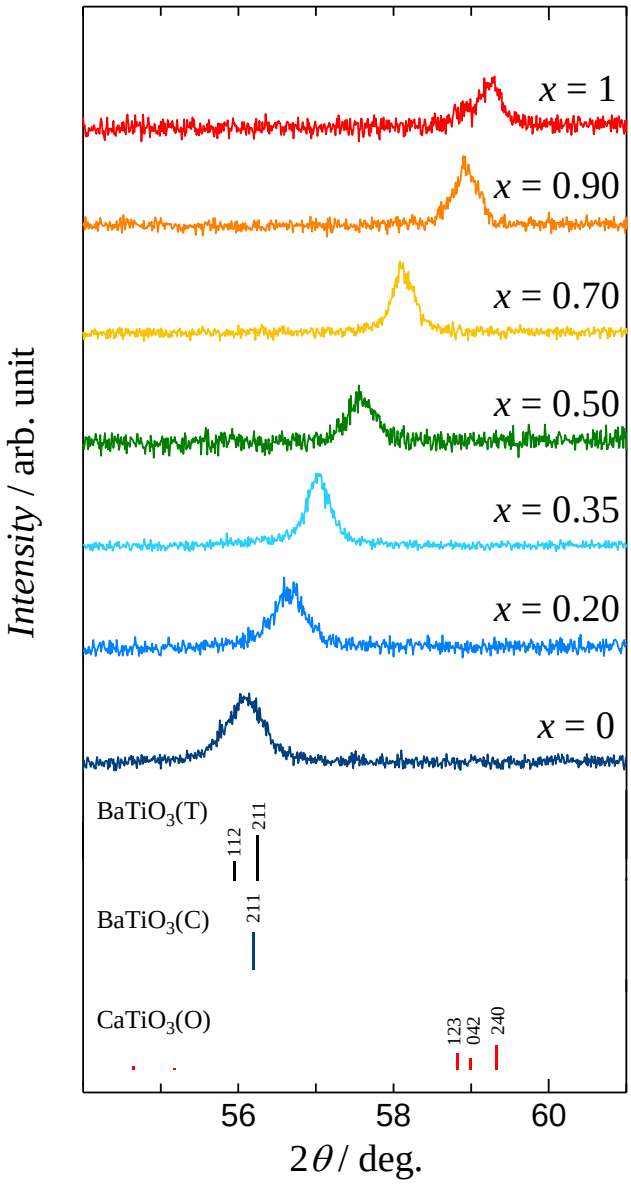

Fig. 2.13 The enlarged view of the XRD patterns of the annealed film samples formed by the sputtering using the $(BaTiO_3)_{1-x}(CaTiO_3)_x$ targets. The lines at the bottom represent the diffraction patterns of tetragonal $BaTiO_3$, cubic $BaTiO_3$ and orthorhombic $CaTiO_3$.

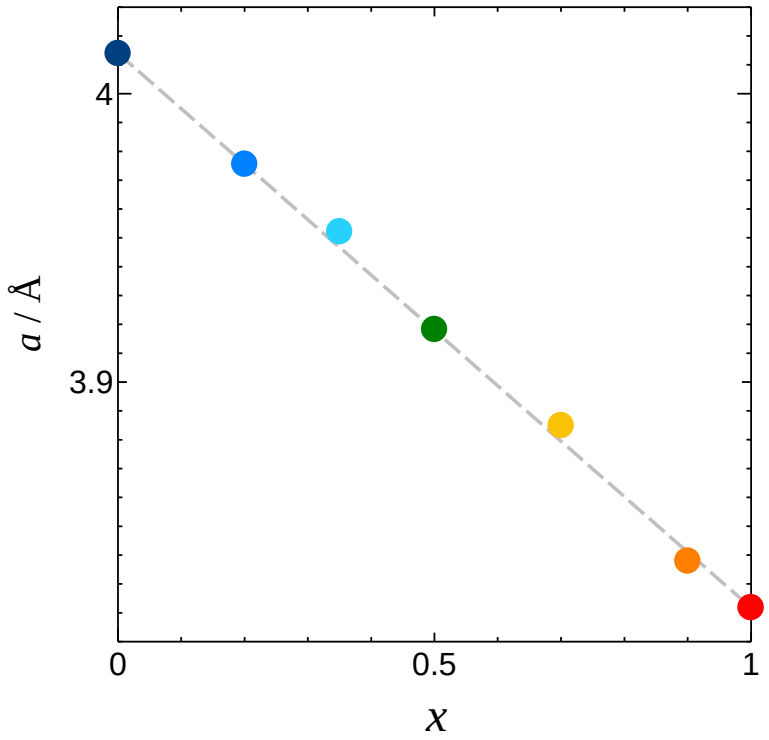

Fig. 2.14　Dependence of the lattice constants a of the crystalline film samples on the composition x of the $(BaTiO_3)_{1-x}(CaTiO_3)_x$ targets used in the sputtering.

Table 2.5 Mole fraction of $CaTiO_3$ in $Ba_{1-x}Ca_xTiO_3$ solid solutions x, and experimental values of lattice constants a of the solid solutions at temperature T = 298.15 K and pressure p = 0.1 MPa,[a] and standard uncertainties u of x and a

x	a / Å	$u(x)$	$u(a)$ / Å
0 ($BaTiO_3$)	4.014	--	0.0002
0.20	3.976	0.017	0.0033
0.35	3.952	0.017	0.0033
0.50	3.918	0.017	0.0033
0.70	3.885	0.017	0.0033
0.90	3.838	0.017	0.0033
1 ($CaTiO_3$)	3.822	--	0.0030

[a] Standard uncertainties u are $u(T)$ = 1 K and $u(p)$ = 10 kPa.

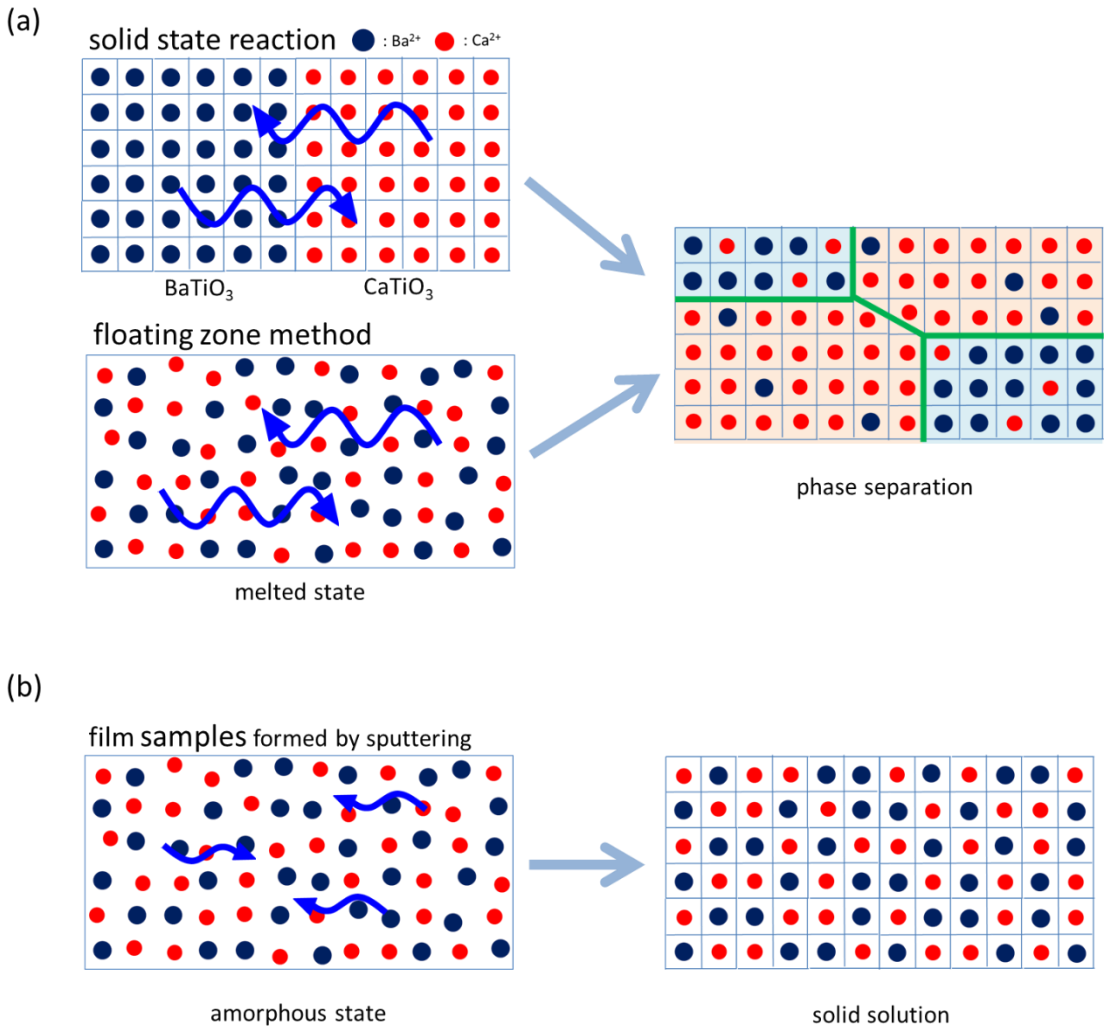

Fig. 2.15 Formation mechanism of solid solutions without miscibility gap: (a) Phase separation occurs in solid-state reaction and floating zone method by long-range diffusion of constituting ions; (b) $Ba_{1-x}Ca_xTiO_3$ solid solutions are formed by 'sputter-anneal' method, in which only short-range diffusion is allowed for the ions.

2.3.2. Dielectric properties of $Ba_{1-x}Ca_xTiO_3$ solid solutions

To investigate Ca composition dependence of the permittivity in $Ba_{1-x}Ca_xTiO_3$ film samples, I examined the formation of the amorphous and solid-solution film samples on the $SrTiO_3$:Nb single-crystal substrates, which have electrical conductivity and can be used as the electrodes in the dielectric measurements. A photograph of the as-prepared film sample formed on the $SrTiO_3$:Nb substrate by the sputtering with using the $(BaTiO_3)_{0.50}(CaTiO_3)_{0.50}$ target is shown in Fig. 2.16(a). Fig. 2.16(b) is a surface image and roughness profile of the as-prepared film sample observed by the laser scanning microscope. As shown in Fig. 2.16(b), the surface of the film sample is rather flat and smooth. As-prepared film samples exhibited halo patterns at around $2\theta = 30°$ in the XRD experiments (Fig.2.17) and were confirmed to have amorphous structure as in the cases using the quartz glass substrates.

Fig. 2.18 shows relations between electric flux density (D) and electric field (E) of amorphous film samples obtained by the Sawyer-Tower circuit [24] at 25 ± 1 °C and 1 kHz field frequency. Relative dielectric constants, which are denoted as dielectric constants hereafter in this thesis, ε of the samples were evaluated by the following relations [30]:

$$C = \varepsilon\varepsilon_0 S d^{-1} \qquad \text{eq. (2.3)}$$

here d is thickness of the sample (m), C is capacitance of the sample (F), ε is dielectric constant of the sample, ε_0 is dielectric constant of vacuum ($= 8.854 \times 10^{-12}$ F·m^{-1}), and S is area of the electrode (m^2). Fig. 2.19 shows the Ca composition, x, dependence of the dielectric constants of amorphous $Ba_{1-x}Ca_xTiO_3$ film samples at 1 kHz. To check the reproducibility of the dielectric constants of the samples, I prepared several samples

separately for each Ca composition and carried out the $D-E$ measurements. The error bars in the figure represent the standard deviations of the estimated dielectric constants for each Ca-composition sample. The values of the ε were around 14 ~ 16, and no clear dependence on the Ca composition was observed in these dielectric constants. The evaluated value of ε for the $x = 0$ ($BaTiO_3$) sample agreed well with the reported values [31-33].

To form the $Ba_{1-x}Ca_xTiO_3$ solid solutions on the $SrTiO_3$:Nb single-crystal substrates, I annealed the amorphous film samples at 800 °C for 3 h. Crystallization of the samples proceeded by the annealing also on the substrates. XRD results (Fig.2.20) showed the formation of $Ba_{1-x}Ca_xTiO_3$ solid solutions in whole the Ca composition range of $0 \leq x \leq 1$: All the samples exhibited diffraction peaks attributable to $Ba_{1-x}Ca_xTiO_3$ solid solutions having cubic structures without phase separation nor formation of byproduct on the $SrTiO_3$:Nb single crystals, and the peak positions shifted continuously to higher angles with the Ca composition x. There was no difference exceeding the experimental error in the peak positions between the samples formed on the quartz glass substrates and those on the $SrTiO_3$:Nb single-crystal substrates, indicating that the lattice constants of the formed solid solutions were not affected by the substrates. Fig. 2.21(a) is a photograph of the annealed $Ba_{0.50}Ca_{0.50}TiO_3$ film sample formed on $SrTiO_3$:Nb single crystal substrate, and Fig. 2.21(b) is a surface image and roughness profile of the annealed film sample observed by the laser scanning microscope. No crack was observed in the annealed sample on the $SrTiO_3$:Nb single-crystal substrate differently from that on the quartz glass substrate by the matching of thermal expansion coefficients between the film sample and the substrate [25,34], and the roughness of the surface of the samples was estimated to be within ±25 nm.

In dielectric measurements using a Sawyer-Tower circuit [24] at 25 ± 1 °C, the solid-solution film samples showed linear D−E relations without hysteresis and were found to be paraelectric. That was also in the film sample of $BaTiO_3$ (Fig. 2.22), which is ferroelectric at the temperature in a bulk crystal. The crystallites composing the film sample of $BaTiO_3$ have a cubic structure as mentioned above, and the origin of the structure and the paraelectricity would be the smallness of the grain size of about 50 nm. Therefore, we applied ac conductivity measurements for the samples using the impedance analyzer. The observed complex admittance Y^* of the samples attached the Pt electrode exhibited frequency dependences. The frequency-dependent Y^* of each sample was well reproduced by assuming a series circuit of the capacitance originated from the crystalline film sample and contact resistance between the film sample and the Pt electrode and possibly the $SrTiO_3$:Nb substrate as shown in Fig. 2.23. Thus, I evaluated dielectric constants of the $Ba_{1-x}Ca_xTiO_3$ solid-solution samples from the capacitances obtained by the analyses according to the Y^* formalism.

As shown in Fig. 2.24, the frequency dependence of the dielectric constants ε was observed to be small within the measured frequency range from 1 to 10^5 Hz in each sample, but the constants changed rather largely with the Ca composition x of the samples. Fig. 2.25 shows the Ca composition, x, dependence of the dielectric constants of $Ba_{1-x}Ca_xTiO_3$ solid-solution samples at 1 kHz, and the measured parameters are listed in Table 2.6. To check the reproducibility of the dielectric constants of the samples, I prepared several samples separately for each Ca composition and carried out the ac conductivity measurements. The error bars in the figure represent the standard deviations of the estimated dielectric constants for each Ca-composition sample. The dielectric

constants ε were observed to increase with the mixing of Ba^{2+} and Ca^{2+} ions, and the sample with $x = 0.35$ showed the highest dielectric constant.

To elucidate the origin of this peculiar dependence of ε on the Ca composition x, I tried to estimate the spaces around Ba^{2+}, Ca^{2+} and Ti^{4+} ions in the solid solutions from the lattice constants shown in Fig. 2.14 and ionic radii of those ions and O^{2-} ion [27]. Among the distances between the metal and nearest neighboring oxygen ions, L(Ba–O), L(Ca–O) and L(Ti–O), estimated from the lattice constants, only the L(Ca–O) in the samples with $x = 0.20$, 0.35, 0.50 and 0.70 were found to have larger values than the sum of the ionic radii of the metal and oxygen ions. Arrangement of constituent ions around Ca^{2+} ion in the unit cell of $Ba_{1-x}Ca_xTiO_3$ solid solutions is shown in Fig. 2.26(a), and the positional relation between the Ca^{2+} ion and the nearest neighboring O^{2-} ions is shown in Fig. 2.26(b). The magnitude of the extra space around Ca^{2+} ions in the samples can be expressed as ΔL, which was evaluated by subtracting the ionic radii of Ca^{2+} and O^{2-} from the L(Ca–O) and shown in Fig. 2.27(a) as a function of the Ca composition x for the $Ba_{1-x}Ca_xTiO_3$ samples. The dielectric response of the $Ba_{1-x}Ca_xTiO_3$ solid solutions is considered to be related largely to the displacement of Ca^{2+} and probably Ti^{4+} ions using the extra space [35, 36], and increment of the amount of the extra space in the crystalline lattice might bring larger dielectric constant for the solid-solution sample. The value of ΔL multiplied by the Ca composition x, $\Delta L \times x$, for the solid-solution sample of $Ba_{1-x}Ca_xTiO_3$ indexes the amount of the extra space in the crystalline lattice of the sample. As shown in Fig. 2.27(b), the value of $\Delta L \times x$ shows a tendency to increase with the mixing of Ba^{2+} and Ca^{2+} ions and exhibits a maximum at around $x = 0.35$. The feature corresponds well to the change of the dielectric constants in $Ba_{1-x}Ca_xTiO_3$ solid solutions with the Ca composition. The image of the extra space expressed by $\Delta L \times x$ around the

Ca^{2+} ions and that of the displacements of Ca^{2+} and Ti^{4+} ions are shown in Fig. 2.28(a) and (b). The displacements of Ca^{2+} and Ti^{4+} ions to the extra space around Ca^{2+} ions in the crystalline lattice are considered to govern the dielectric properties of the solid solutions. The large electrostriction reported for $Ba_{1-x}Ca_xTiO_3$ near the solubility limit in the conventional solid-state reaction of $x \sim 0.23$ [16] is considered to have a deep relationship with the extra space formed around Ca^{2+} ions, as in the dielectric constant observed here.

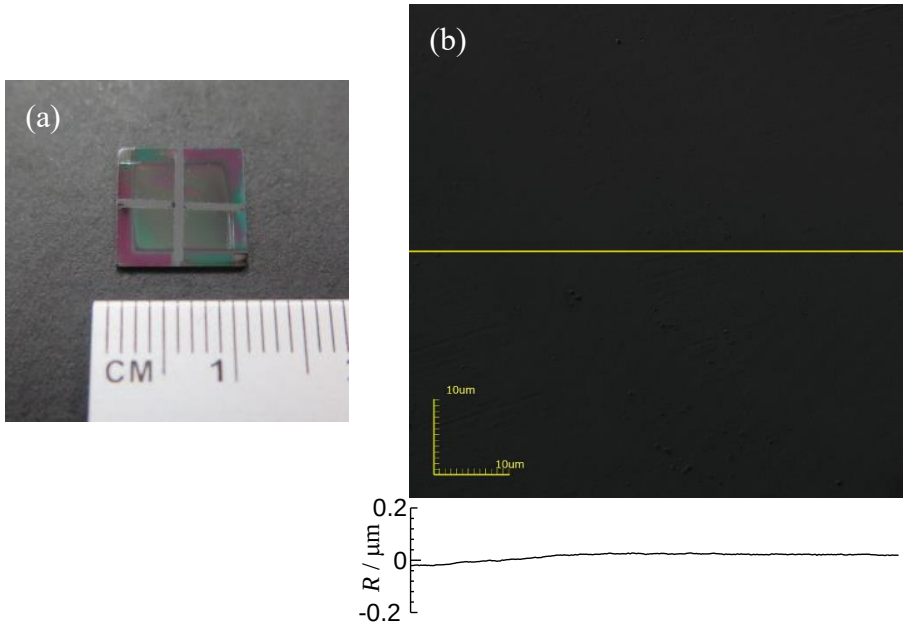

Fig. 2.16 As-prepared film sample deposited on the $SrTiO_3$:Nb substrate by the sputtering with using the $(BaTiO_3)_{0.50}(CaTiO_3)_{0.50}$ target; (a) photograph of the sample, (b) surface image and roughness profile observed by laser scanning microscope. Surface roughness, *R*, was measured along the yellow line indicated in the image.

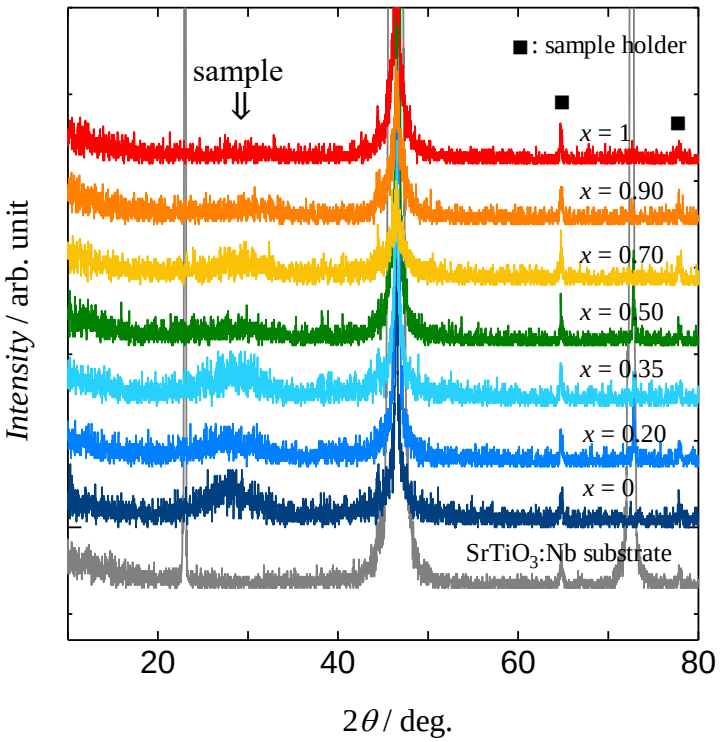

Fig. 2.17　XRD patterns of the as-prepared film samples formed by the rf magnetron sputtering with using the $(BaTiO_3)_{1-x}(CaTiO_3)_x$ targets and that of the $SrTiO_3$:Nb single crystals used as the substrates.

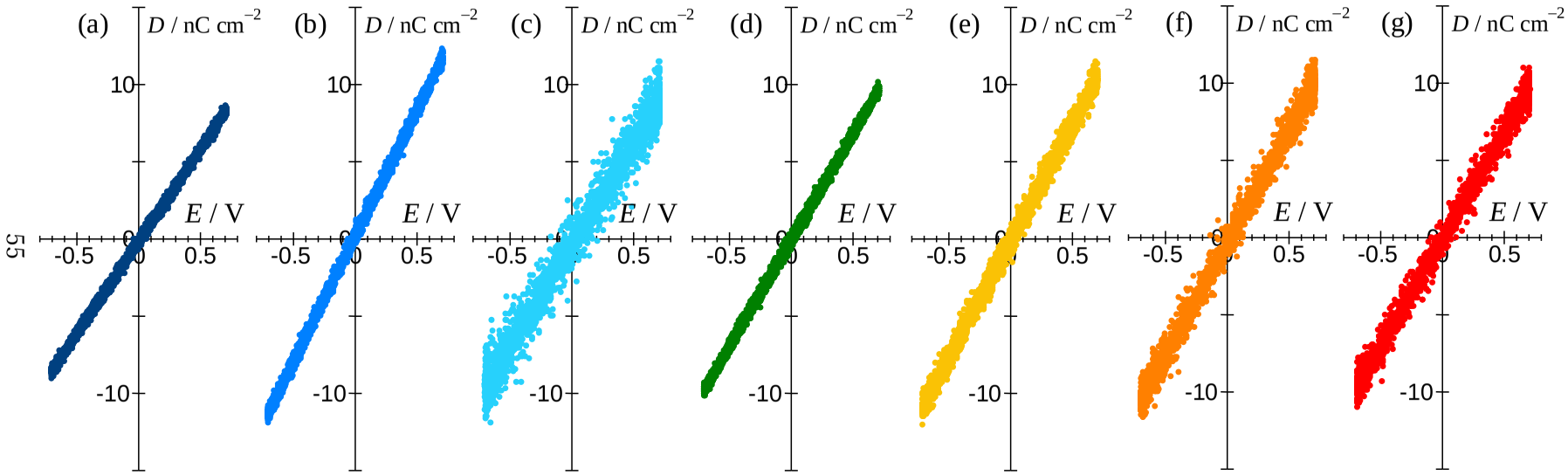

Fig. 2.18 D–E relations of the amorphous $Ba_{1-x}Ca_xTiO_3$ film samples at 1 kHz. (a) $x = 0$, (b) $x = 0.20$, (c) $x = 0.35$, (d) $x = 0.50$, (e) $x = 0.70$, (f) $x = 0.90$, (g) $x = 1$.

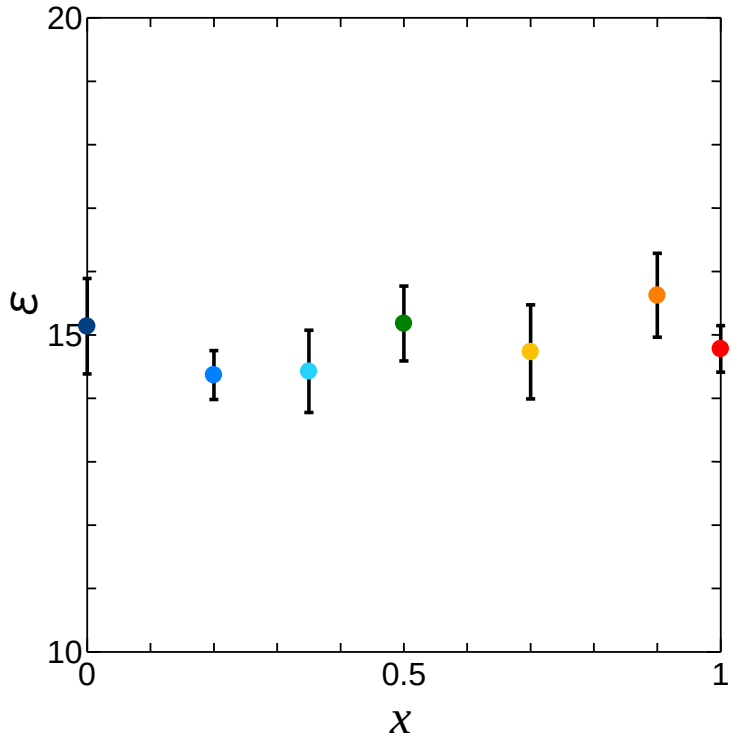

Fig. 2.19 Dielectric constants ε at 1 kHz of the as-prepared $Ba_{1-x}Ca_xTiO_3$ film samples. Error bars represent the standard deviations of the ε evaluated from the results for separately prepared several samples.

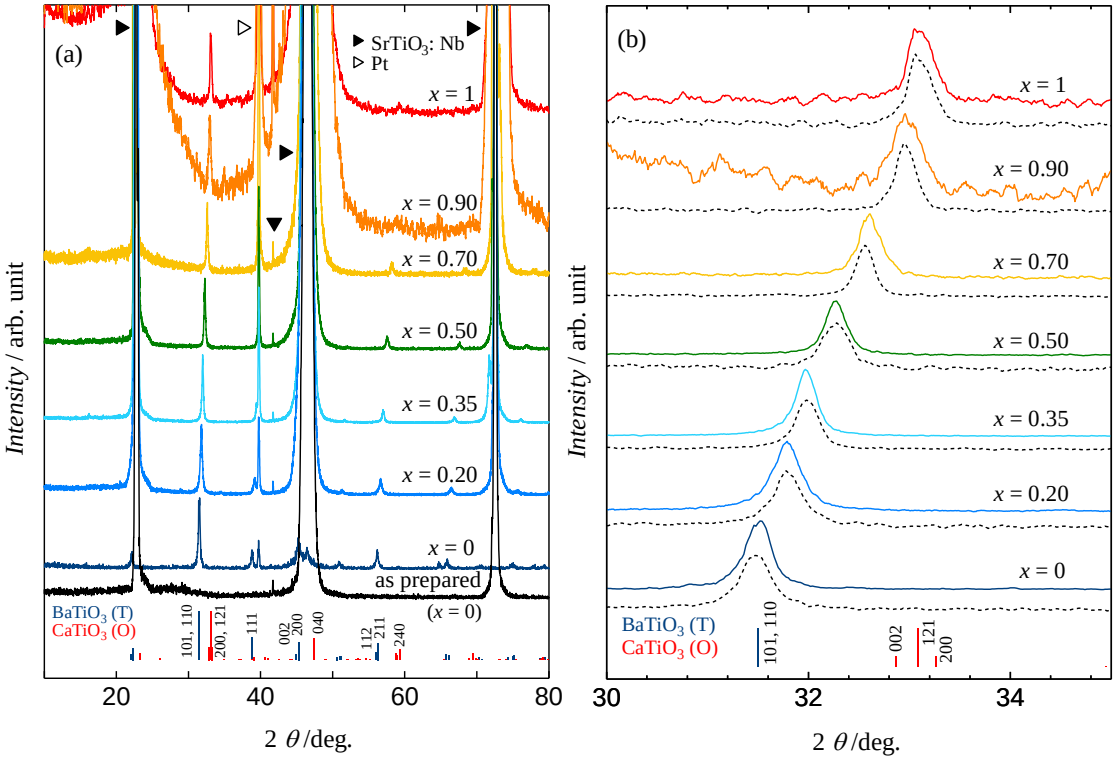

Figure 2.20 XRD patterns of the annealed film samples formed on the $SrTiO_3$:Nb single-crystal substrates by the sputtering with using the $(BaTiO_3)_{1-x}(CaTiO_3)_x$ targets (a), and the enlarged view of the diffractions (b). The diffractions of the annealed film samples formed on the quartz glass substrates are shown by dashed lines in (b) for comparison.

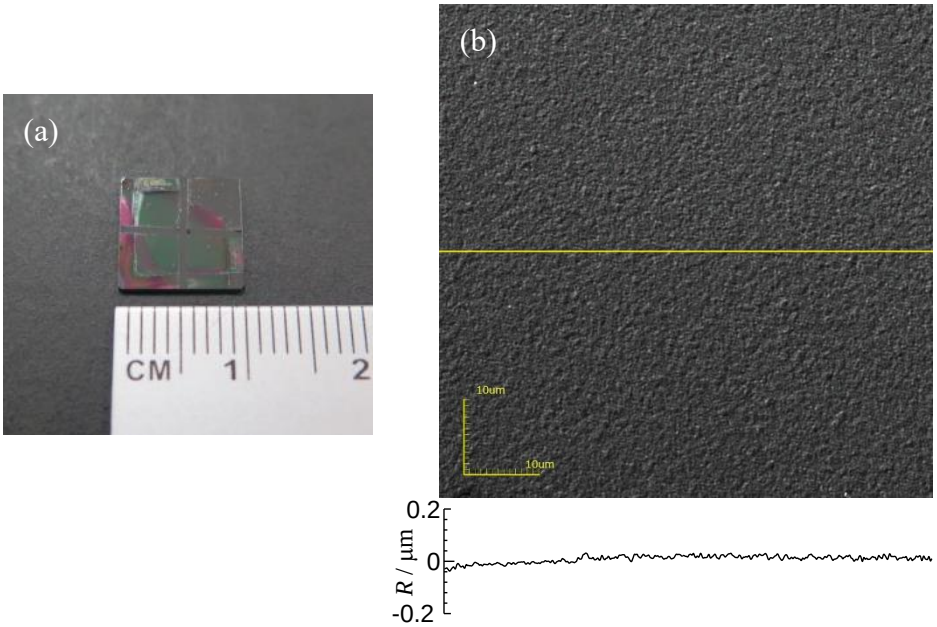

Fig. 2.21 Annealed film sample formed on $SrTiO_3$:Nb substrate by the sputtering with using the $(BaTiO_3)_{0.50}(CaTiO_3)_{0.50}$ target; (a) photograph of the sample, (b) surface image and roughness profile observed by laser scanning microscope. Surface roughness, *R*, was measured along the yellow line indicated in the image.

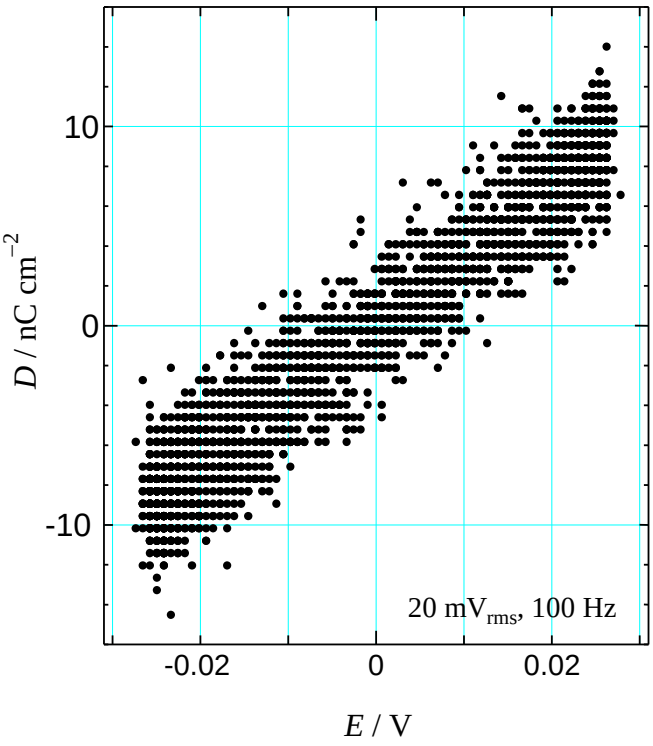

Fig. 2.22 D–E relation of the annealed $BaTiO_3$ film sample.

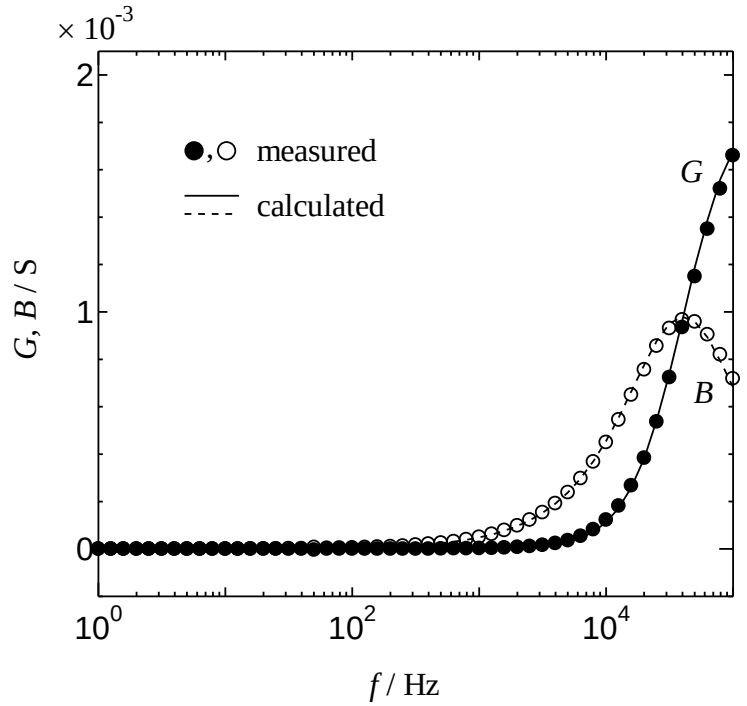

Fig. 2.23 Frequency dependence of the complex admittance Y^* (= $G + iB$; where G is conductance and B is susceptance) for the crystalline $BaTiO_3$ film sample; closed circles and open circles represent the results of G and B, respectively, obtained by the ac conductivity measurement. Solid and dashed lines show the calculated results for G and B by assuming a series circuit of a capacitance C_s = 7.70 nF and a resistance R_s = 510 Ω.

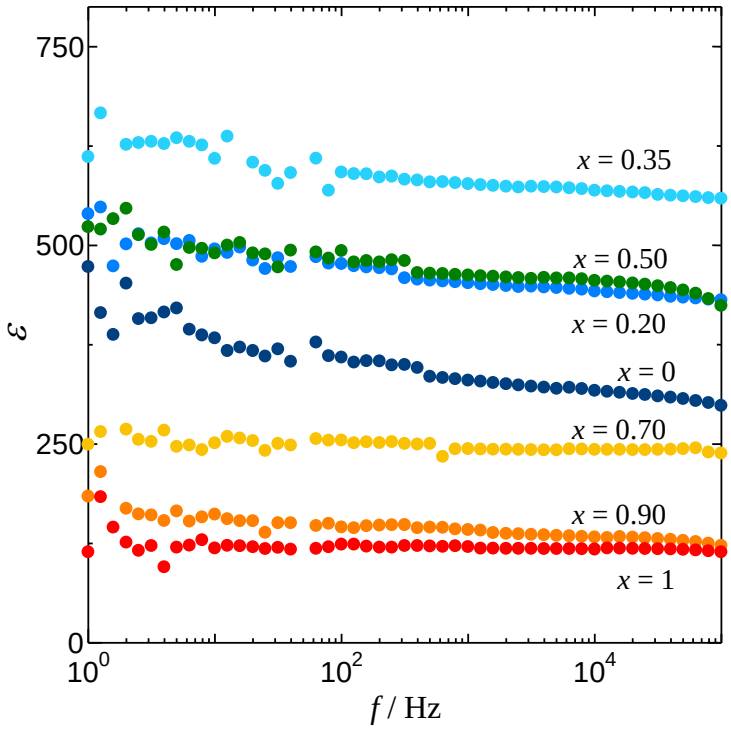

Fig. 2.24 Frequency dependence of the dielectric constants ε of $Ba_{1-x}Ca_xTiO_3$ solid-solution film samples.

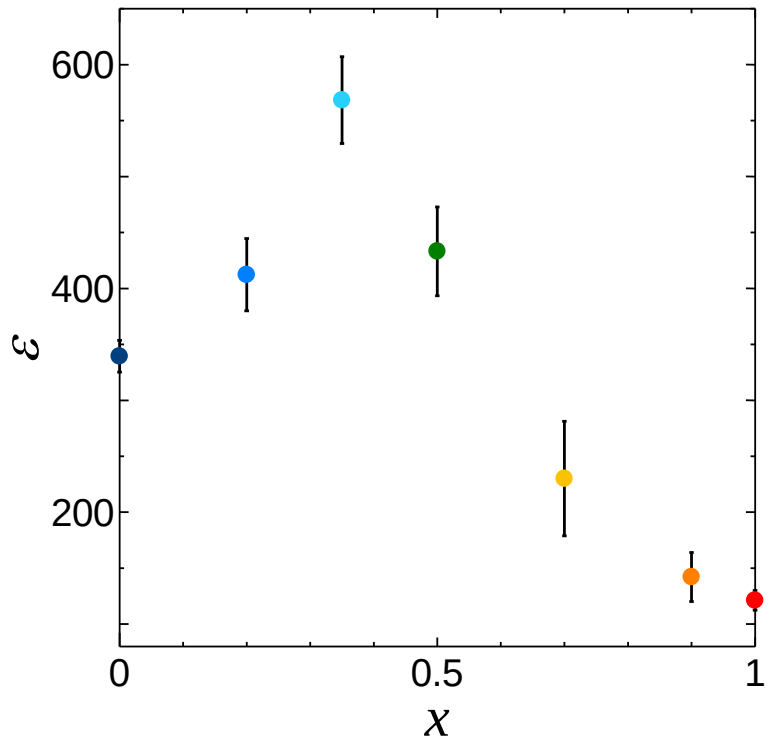

Fig. 2.25　Dielectric constants ε at 1 kHz of the $Ba_{1-x}Ca_xTiO_3$ solid-solution samples. Error bars represent the standard deviations of the ε evaluated from the results for separately prepared several samples.

Table 2.6 Mole fraction of $CaTiO_3$ in $Ba_{1-x}Ca_xTiO_3$ solid solutions x, and experimental values of dielectric constants ε at frequency ν = 1 kHz with oscillating electric field E = 10 mV_{rms} of the solid solutions at temperature T = 298.15 K and pressure p = 0.1 MPa,[a] and standard uncertainties u of x and ε

x	ε	$u(x)$	$u(\varepsilon)$
0 ($BaTiO_3$)	339	--	14.2
0.20	412	0.017	32.3
0.35	568	0.017	38.7
0.50	433	0.017	39.7
0.70	230	0.017	51.2
0.90	142	0.017	21.9
1 ($CaTiO_3$)	121	--	8.7

[a] Standard uncertainties u are $u(\nu)$ = 100 mHz, $u(E)$ = 20 μV_{rms}, $u(T)$ = 1 K and $u(p)$ = 10 kPa.

(a)

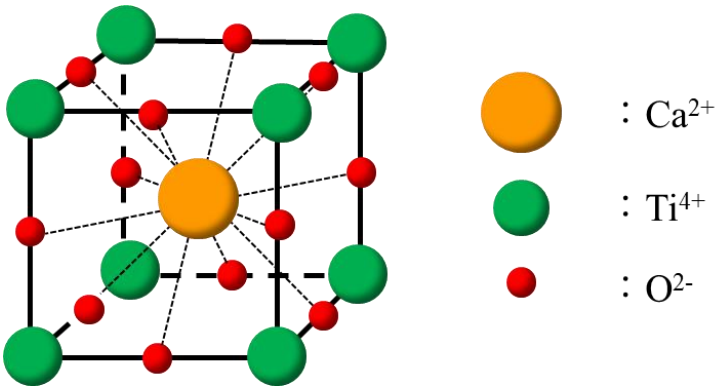

(b)

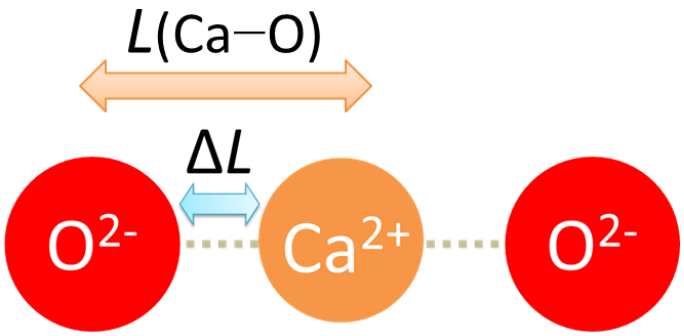

Fig. 2.26 Arrangement of constituent ions around Ca^{2+} ion in the unit cell of $Ba_{1-x}Ca_xTiO_3$ solid solutions (a), and the positional relation between the Ca^{2+} ion and the nearest neighboring O^{2-} ions (b).

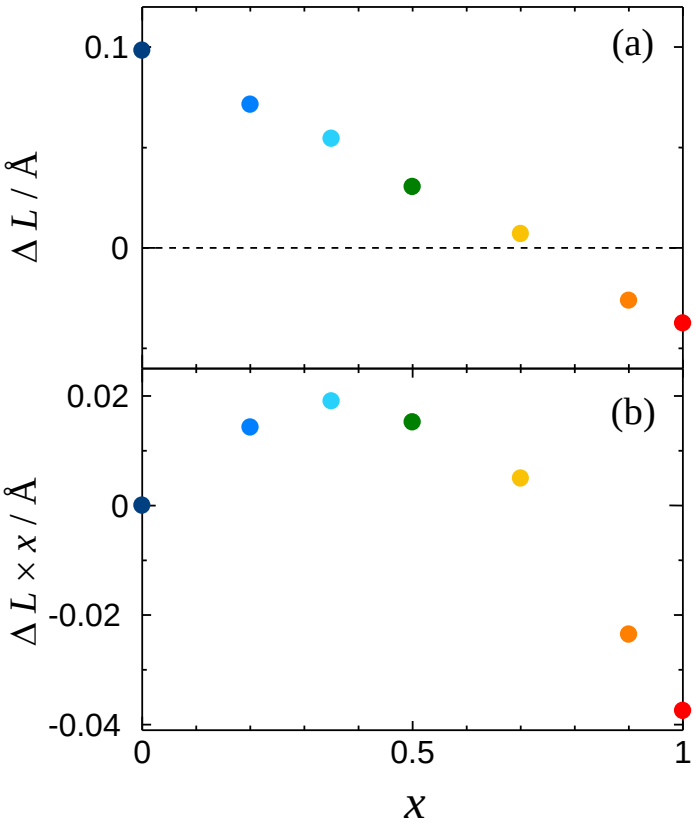

Fig. 2.27 Ca composition x dependence of the extra space around Ca^{2+} ions in the $Ba_{1-x}Ca_xTiO_3$ solid-solution samples; (a) ΔL and (b) $\Delta L \times x$, see text for details. The values for $x = 0$ were estimated by putting Ca^{2+} ion in the Ba^{2+}-ion site imaginarily.

(a)

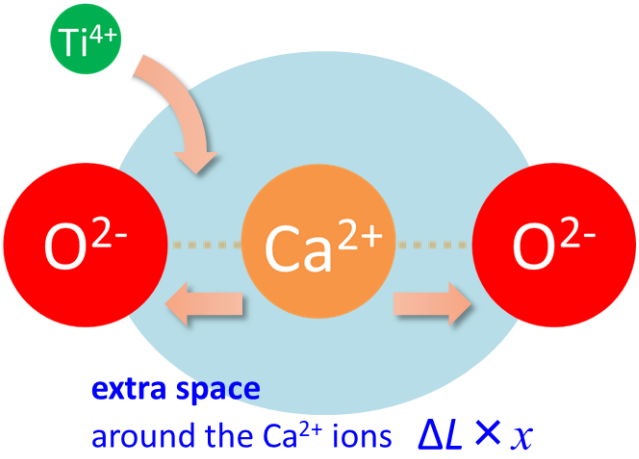

(b)

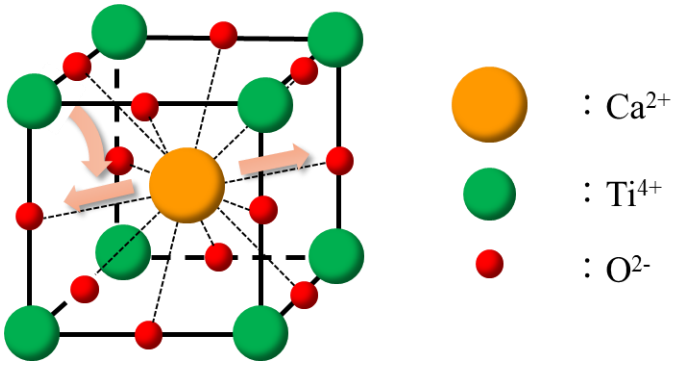

Fig. 2.28 Image of the extra space expressed by $\Delta L \times x$ around the Ca^{2+} ions and that of the displacements of Ca^{2+} and Ti^{4+} ions (a), and the image of the displacements in the crystalline lattice (b).

2.4. Conclusions

In this work, I succeeded in forming $Ba_{1-x}Ca_xTiO_3$ solid solutions beyond the solubility limit reported so far by preparing amorphous film samples by the sputtering and annealing the amorphous samples at the rather low temperature than those used in a conventional solid-state reaction method, which allows only a restricted migration of constituent ions and suppresses the proceeding of phase separations. The dielectric constants ε of the formed solid solutions were observed to increase with the mixing of Ba^{2+} and Ca^{2+} ions, and the sample with $x = 0.35$ showed the highest dielectric constant. This peculiar dependence of the ε on the Ca composition x was well explained by the formation of extra space around Ca^{2+} ions substituted for Ba^{2+} ions, and the displacements of Ca^{2+} and probably Ti^{4+} ions using the space were understood to affect largely the dielectric properties of $Ba_{1-x}Ca_xTiO_3$ solid solutions.

References

[1] G. H. Haertling, Ferroelectric Ceramics: History and Technology, J. Am. Ceram. Soc. 82 (1999) 797–818. https://doi.org/10.1111/j.1151-2916.1999.tb01840.x

[2] S. T. McKinstry, C. A. Randall, Movers, shakers, and storers of charge: The legacy of ferroelectricians L. Eric Cross and Robert E. Newnham, J. Am. Ceram. Soc. 100 (2017) 3346–3359. https://doi.org/10.1111/jace.15021

[3] E. J. H. Lee, F. M. Pontes, E. R. Leite, E. Longo, R. Magnani, P. S. Pizani, J. A. Varela, Effects of post-annealing on the dielectric properties of Au/$BaTiO_3$/Pt thin film capacitors, Mater. Lett. 58 (2004) 1715–1721. https://doi.org/10.1016/j.matlet.2003.10.047

[4] K. C. Singh, A. K. Nath, Barium titanate nanoparticles produced by planetary ball milling and piezoelectric properties of corresponding ceramics, Mater. Lett. 65 (2011) 970–973. https://doi.org/10.1016/j.matlet.2010.12.039

[5] C. X. Li, B. Yang, S. T. Zhang, R. Zhang, Y. Sun, J. J. Wang, R. X. Wang, W. W. Cao, Phase transition, microstructure and electrical properties of Fe doped $Ba_{0.70}Ca_{0.30}TiO_3$ lead-free piezoelectric ceramics, Ceram. Int. 39 (2013) 8701–8708. https://doi.org/10.1016/j.ceramint.2013.04.052

[6] P. Jaiban, A. Watcharapasorn, Effects of Mg doping on electrical properties of $Ba_{0.7}Ca_{0.3}TiO_3$ ceramics, Mater. Today Commun. 11 (2017) 184–190. https://doi.org/10.1016/j.mtcomm.2017.05.001

[7] T. Mitsui, W. B. Westphal, Dielectric and X-Ray Studies of $Ca_xBa_{1-x}TiO_3$ and $Ca_xSr_{1-x}TiO_3$, Phys. Rev. 124 (1961) 1354–1539. https://doi.org/10.1103/PhysRev.124.1354

[8] R. Varatharajan, S. B. Samanta, R. Jayavel, C. Subramanian, A. V. Narlikar, P. Ramasamy, Ferroelectric characterization studies on barium calcium titanate single crystals, Materials Characterization 45 (2000) 89–93. https://doi.org/10.1016/S1044-5803(00)00053-X

[9] M. McQuarrie, Structural Behavior in the System (Ba, Ca, Sr)TiO_3 and Its Relation to Certain Dielectric Characteristics, J. Am. Ceram. Soc. 38 (1955) 444–449. https://doi.org/10.1111/j.1151-2916.1955.tb14571.x

[10] R. C. DeVries, R. Roy, Phase Equilibria in the System $BaTiO_3$-$CaTiO_3$, J. Am. Ceram. Soc. 38 (1955) 142–146. https://doi.org/10.1111/j.1151-2916.1955.tb14918.x

[11] D. Fu, M. Itoh, S. Koshihara, Invariant lattice strain and polarization in $BaTiO_3$–$CaTiO_3$ ferroelectric alloys, J. Phys.: Condens. Matter 22 (2010) 052204. https://doi.org/10.1088/0953-8984/22/5/052204

[12] R. C. Pullar, Y. Zhang, L. Chen, S. Yang, J. R. G. Evans, A. N. Salak, D. A. Kiselev, A. L. Kholkin, V. M. Ferreira, N. M. Alford, Dielectric measurements on a novel $Ba_{1-x}Ca_xTiO_3$ (BCT) bulk ceramic combinatorial library, J. Electroceram. 22 (2009) 245–251. https://doi.org/10.1007/s10832-008-9430-5

[13] F. I. Hussain, F. M. Tuamaa, Effect of Ca Substitution on Structural properties of $Ba_{1-x}Ca_xTiO_3$ Nano Compound Synthesis by Sol-Gel Method, Int. J. Adv. Res. Sci. Eng. Tech. 3 (2016) 1884–1888.

[14] D. Fu, M. Itoh, S. Koshihara, T. Kosugi, S. Tsuneyuki, Anomalous Phase Diagram of Ferroelectric (Ba,Ca)TiO_3 Single Crystals with Giant Electromechanical Response, Phys. Rev. Lett. 100 (2008) 227601. https://doi.org/10.1103/PhysRevLett.100.227601

[15] Q. Jia, B. Shen, X. Hao, S. Song, J. Zhai, Anomalous dielectric properties of $Ba_{1-x}Ca_xTiO_3$ thin films near the solubility limit, Mater. Lett. 63 (2009) 464–466. https://doi.org/10.1016/j.matlet.2008.11.026

[16] X. Wang, H. Yamada, C. N. Xu, Large electrostriction near the solubility limit in $BaTiO_3$–$CaTiO_3$ ceramics, Appl. Phys. Lett. 86 (2005) 022905. https://doi.org/10.1063/1.1850598

[17] X. Cheng, M. Shen, Different microstructure and dielectric properties of $Ba_{1-x}Ca_xTiO_3$ ceramics and pulsed-laser-ablated films, Mater. Res. Bull. 42 (2007) 1662–1668. https://doi.org/10.1016/j.materresbull.2006.11.033

[18] A. Purwanto, D. Hidayat, Y. Terashi, K. Okuyama, Synthesis of Monophasic $Ca_xBa_{(1-x)}TiO_3$ Nanoparticles with High Ca Content (x > 23%) and Their Photoluminescence Properties, Chem. Mater. 20 (2008) 7440–7446. https://doi.org/10.1021/cm802524e

[19] R. V. Stuart, Vacuum Technology, Thin Films, and Sputtering An Introduction, ACADEMIC PRESS, INC., London, 1983, pp. 130–131.

[20] P. Gonon, F. E. Kamel, Dielectric response of Cu/amorphous $BaTiO_3$/Cu capacitors, J. Appl. Phys. 101 (2007) 073901. https://doi.org/10.1063/1.2716871

[21] R. C. Rau, Applicability of Routine Method of Crystallite Size Analysis, Advances in X-ray Analysis 6 (1962) 191–201. https://doi.org/10.1154/S0376030800002068

[22] R. C. Rau, Routine Crystallite-size Determination by X-ray Diffraction Line Broadening, Advances in X-ray Analysis 5 (1961) 104–115. https://doi.org/10.1154/S0376030800001476

[23] B. D. Culluty, Elements of X-ray Diffraction, second ed., Addison-Wesley, Massachusetts, 1978, pp. 99–103.

[24] C. B. Sawyer, C. H. Tower, Rochelle Salt as a Dielectric, Phys. Rev. 35 (1930) 269–273. https://doi.org/10.1103/PhysRev.35.269

[25] NEOTRON CO., LTD, http://www.neotron.co.jp/crystal/1/BaTiO3.html

[26] Shin-Etsu Quartz Products Co., Ltd., Technology Guide 1 (2018) p. 8. https://www.sqp.co.jp/catalog/images/Technology_Guide1_j.pdf

[27] R. D. Shannon, Revised effective ionic radii and systematic studies of interatomic distances in halides and chalcogenides, Acta Cryst. A 32 (1976) 751–767. https://doi.org/10.1107/S0567739476001551

[28] H. Miura, CellCalc: A unit cell parameter refinement program on Windows computer, J. Cryst. Soc. Jpn. 45 (2003) 145–147. https://doi.org/10.5940/jcrsj.45.145

[29] L. Vegard, Die Konstitution der Mischkristalle und die Raumfüllung der Atome, Z. Phys. 5 (1921) 17–26. https://doi.org/10.1007/BF01349680

[30] The Chemical Society of Japan, Encyclopedia of Experimental Chemistry, 4th ed., Maruzen, 1991, pp. 215–218.

[31] F. El Kamel, P. Gonon, F. Jomni, Electrical properties of low temperature deposited amorphous barium titanate thin films as dielectrics for integrated capacitor, Thin Solid Films 504 (2006) 201–204. https://doi.org/10.1016/j.tsf.2005.09.125

[32] D. J. McClure, J. R. Crowe, Characterization of amorphous barium titanate films prepared by rf sputtering, J. Vac. Sci. Technol. 16 (1979) 311–314. https://doi.org/10.1116/1.569934

[33] K. Sreenivas, A. Mansingh, M. Sayer, Structural and electrical properties of rf-sputtered amorphous barium titanate thin films, J. Appl. Phys. 62 (1987) 4475–4481. https://doi.org/10.1063/1.339037

[34] Furuuchi Chemical, http://www.furuchi.co.jp/crystal/srtio3.html.

[35] H. Tanaka, H. Tabata, K. Ota, T. Kawai, Molecular-dynamics prediction of structural anomalies in ferroelectric and dielectric $BaTiO_3$-$SrTiO_3$-$CaTiO_3$ solid solutions, Phys. Rev. B 53 (1996) 14112–14116. https://doi.org/10.1103/PhysRevB.53.14112

[36] I. Levin, V. Krayzman, J. C. Woicik, Local-structure origins of the sustained Curie temperature in (Ba,Ca)TiO_3 ferroelectrics, Appl. Phys. Lett. 102 (2013) 162906. https://doi.org/10.1063/1.4802996

Chapter 3. Application of 'sputter-anneal' method to $Ba_{1-x}Ca_xZrO_3$ system and dielectric properties of $Ba_{1-x}Ca_xZrO_3$ solid solutions

Abstract

Formation of solid solutions was examined in a wide miscibility gap system of $Ba_{1-x}Ca_xZrO_3$ by the 'sputter-anneal' method, in which amorphous film samples were prepared by rf magnetron sputtering and annealed successively at a moderate temperature condition. $Ba_{1-x}Ca_xZrO_3$ solid solutions were formed successfully by the method as monophasic products in whole the composition range of $0 < x < 1$, indicating the usefulness and the validity of the method for the formation of solid solutions in perovskite-type oxides, and Ca composition dependence of the dielectric constants ε was revealed in the solid-solution system.

3.1. Introduction

Complex oxides with a perovskite-type structure are important and potential materials as dielectric substances, catalysts, ion conductors, and so on [1-7], and their physical and chemical properties are often controlled and optimized by varying compositions [1-5]. The extension of the solubility limit would bring information of value to understand the dependence of their properties on the compositions and open new possibilities for them as functional materials. Sputtering is a valuable method to form film samples of oxides, and formed samples on to substrates at low temperatures usually have amorphous structures [8]. The formed amorphous film samples, in which the constituent ions disperse homogeneously, are considered to be able to crystallize only by short-range diffusion of the ions when annealed. The sputtering and successive annealing, thus, have a high possibility of producing solid solutions of oxides in wide composition range, avoiding the occurrence of phase separations. Actually, as described in Chapter 2, I have succeeded in forming $Ba_{1-x}Ca_xTiO_3$ solid solutions with Ca compositions within the miscibility gap by preparing amorphous film samples with the help of rf magnetron sputtering and annealing the samples at relatively low temperature [9]. The 'sputter-anneal' method is expected from its simplicity to be useful and widely applicable for producing solid solutions in oxide systems. Therefore, I examined the formation of solid solutions by the sputter-anneal method in $Ba_{1-x}Ca_xZrO_3$ system, which has been actively studied as an attractive candidate for use in microwave applications [2-4] and has a wide miscibility gap of $0.03 < x < 0.99$ [2], and tried to obtain the information about the composition dependence of their dielectric properties in wide composition range.

3.2. Experimental section

The powder samples of $Ba_{1-x}Ca_xZrO_3$ (x = 0, 0.25, 0.50, 0.75 and 1) were prepared by calcining raw materials of $BaCO_3$, $CaCO_3$ and ZrO_2 weighed to the desired compositions at 1000 °C for 12 h. Then the samples were pressed into disks, sintered at 1400 °C for 6 h, and shaped to targets for sputtering (1 inchϕ, 2 mm$t$). The details of the samples used are given in Table 3.1, and photographs of a typical sample of the sintered disks and that of the targets set to the holder for sputtering are shown in Fig. 3.1. The densities and sintering degree of the prepared targets are listed in Table 3.2. $Ba_{1-x}Ca_xZrO_3$ film samples were deposited on quartz glass substrates (10 mm × 10 mm × 0.8 mm$t$) at room temperature by using the targets and a conventional upward type rf magnetron sputtering apparatus (ULVAC, SCOTT-C3-T1) under Ar (1.0 Pa) / O_2 (0.4 Pa) mixed gas atmosphere. The thicknesses of the film samples were controlled to be ~1 μm by setting the sputtering time between 6 and 8 h. Annealing of the film samples was performed under atmospheric condition by using an electric furnace.

X-ray diffraction (XRD) experiments were carried out with a powder X-ray diffractometer (Rigaku, RINT2200VF) by using Cu Kα radiation. Measurement conditions in the XRD are listed in Table 3.3. Morphology observation and elemental analysis of the surfaces of the $Ba_{0.50}Ca_{0.50}ZrO_3$ target and the annealed film sample formed by using the target were performed with a scanning electron microscope (SEM) equipped an energy dispersive X-ray (EDX) spectrometer (SHIMADZU, SSX-550 + SEDX-500). The surface of the samples was coated with Au-Pd in ~3-nm thick by using a magnetron sputtering apparatus (VACUUM DEVICE, MSP-1S), and the measurements

were done under accelerating voltage of 30 kV. Dielectric measurements were performed using the impedance analyzer with the electrochemical interface described in Chapter 2 (§2.2) in the frequency range 10^2–10^5 Hz by applying the oscillating electric field of 10 mV_{rms}.

Table 3.1 List of chemicals used, their source and purity

Chemicals	Source	Purity	Analysis method
$BaCO_3$	Wako Pure Chemical Industries	0.999[a]	Manufacturer assay
$CaCO_3$	Kanto Kagaku	0.9999[a]	Manufacturer assay
ZrO_2	Soekawa Chemicals	0.999[a]	Manufacturer assay
$(BaZrO_3)_{1-x}(CaZrO_3)_x$; x = 0, 0.25, 0.50, 0.75 and 1	Synthesized in this study	0.99[b]	XRD[c]
Argon	Kansan Corporation	0.9999[a]	Manufacturer assay
Oxygen	Kansan Corporation	0.995[a]	Manufacturer assay
Platinum	Furuya Metal Co., Ltd.	0.999[a]	Manufacturer assay

[a] Mass fraction purity.

[b] The lowest estimation of mole fraction purity.

[c] X-ray diffractometry (Fig. 3.2).

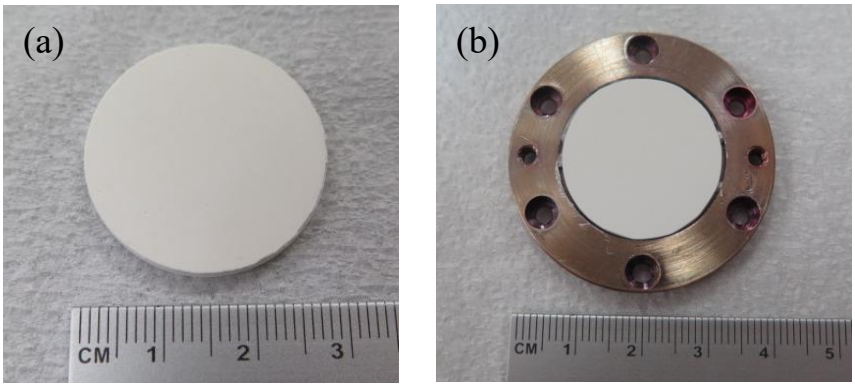

Fig. 3.1 Photograph of a typical sample of the sintered disks (a), and that of the targets set to the holder of the sputtering apparatus (b).

Table 3.2 Densities and sintering degrees of the $Ba_{1-x}Ca_xZrO_3$ targets

Ca composition x	Theoretical density (g cm^{-3})	Density (g cm^{-3})	Sintering degree (%)
0	5.52	3.84	69.6
0.25	5.42	3.69	68.1
0.50	5.32	3.14	59.0
0.75	5.21	2.65	50.9
1	5.11	2.48	48.4

Table 3.3 Measurement conditions in XRD experiments

Measuring method	Continuous mode	Fixed time mode
Scanning axis	θ / 2θ	θ / 2θ
Initial angle (°)	10.000	10.000
Final angle (°)	80.000	80.000
Sampling width (°)	0.02	0.010
Scanning speed (°/ min)	4.000	–
Gate time (sec)	–	1.0
X-ray tube voltage (kV)	40	40
X-ray tube current (mA)	20	20

3.3. Results and discussions

3.3.1. Formation of $Ba_{1-x}Ca_xZrO_3$ solid solutions

Fig. 3.2 shows the results of the XRD experiments for $Ba_{1-x}Ca_xZrO_3$ targets used in the sputtering along with the XRD patterns of $BaZrO_3$ (ICDD No 00-006-0399) and $CaZrO_3$ (ICDD No 00-035-0790). The x = 0 ($BaZrO_3$) and x = 1 ($CaZrO_3$) targets gave the diffraction patterns well corresponding to those reported for $BaZrO_3$ and $CaZrO_3$, respectively. The targets with the Ca compositions x = 0.25, 0.50 and 0.75 exhibited the patterns by the coexistence of Ba-rich and Ca-rich phases of the zirconate as the indication of the phase separation occurred in the preparation process, the calcination and the sintering, of the targets.

Fig. 3.3(a) is a photograph of a typical sample of the as-prepared films deposited on the quartz glass substrate by the sputtering using the $(BaZrO_3)_{0.50}(CaZrO_3)_{0.50}$ target, and Fig. 3.3(b) is a surface image and roughness profile of the as-prepared film sample observed by the laser scanning microscope. As shown in Fig. 3.3(b), the surface of the film sample is rather flat and smooth. In the XRD experiment, the sample exhibited broadened halo patterns characteristic of amorphous structure at around 2θ = 30° overlapped with the diffraction due to the quartz glass substrate, as shown in Fig. 3.4.

To obtain the information about crystallization of the amorphous film samples by annealing, I attempted annealing the as-prepared film sample at temperatures from 400 to 1000 °C for 3 h. The XRD patterns of the annealed samples were also shown in Fig. 3.4 along with the patterns of cubic $BaZrO_3$ and orthorhombic $CaZrO_3$. Diffraction peaks

attributable to the crystallites of the solid solution started to appear by the annealing at 600 °C. The intensity of the diffraction peaks increased with the rise of the annealing temperature up to 800 °C, then signs of occurrence of the phase separation and formation of byproducts were observed by annealing at 1000 °C. In the cases of $BaZrO_3$ and $CaZrO_3$, as-prepared samples by the sputtering exhibited halo patterns characteristic of amorphous structure at around $2\theta = 30°$ in the XRD experiments as shown in Fig. 3.5 and Fig. 3.6, respectively. The as-prepared $BaZrO_3$ film sample started to crystallize by the annealing at 600 °C, crystallization proceeded more efficiently at 800 °C and the formation of byproducts was observed at 1000 °C as shown in Fig. 3.5, as in the case of the film sample formed from the $(BaZrO_3)_{0.50}(CaZrO_3)_{0.50}$ target. In the as-prepared $CaZrO_3$ film sample, as shown in Fig. 3.6, diffraction peaks attributable to the formation of calcia-stabilized zirconia ($Ca_{0.15}Zr_{0.85}O_{1.85}$) [6,10] were observed by the annealing at 600 and 1000 °C. On the other hand, only the diffraction peaks of $CaZrO_3$ were observed by the annealing at 800 °C without the formation of the byproduct. Therefore, the annealing temperature and the duration were decided to be 800 °C and 3 h for the system of $Ba_{1-x}Ca_xZrO_3$.

Fig. 3.7 shows the XRD patterns of the as-prepared film samples by the sputtering and the annealed samples at 800 °C for 3 h. The as-prepared samples with x = 0.25 and 0.75 exhibited halo patterns, as the samples with x = 0, 0.50 and 1, at around 2θ = 30° overlapped with the diffraction by the quartz glass substrate, indicating that all the as-prepared film samples have amorphous structures produced by the rapid quenching of the sputtered clusters on the substrates. The annealed samples, on the other hand, exhibited diffraction peaks showing that the crystallization proceeded in the amorphous film samples at the rather low temperature of 800 °C. Fig. 3.8(a) is a photograph of the annealed film sample formed on the quartz glass substrate by the sputtering with using

the $(BaZrO_3)_{0.50}(CaZrO_3)_{0.50}$ target, and Fig. 3.8(b) is a surface image and roughness profile of the annealed film sample observed by the laser scanning microscope. Mechanical cracks were generated in the annealed sample on the quartz glass substrates, probably due to the mismatch of thermal expansion coefficients between the film sample and the substrate [11,12]. The longer annealing for 6 h at 800 °C in the $x = 0.50$ sample did not affect the area intensities of the diffraction peaks nor the diffraction pattern, as shown in Fig. 3.9, and thus the crystallization of the samples is considered to complete within 3 h. Although the samples with $x = 0.25$, 0.50 and 0.75 have compositions out of the solubility limit of the $Ba_{1-x}Ca_xZrO_3$ system in the conventional solid-state reaction, the diffraction pattern of the crystallized film samples (Fig. 3.7) showed no peak splitting by the coexistence of Ba-rich and Ca-rich phases differently from the targets (Fig. 3.2). The enlarged view of the diffractions of the annealed samples is shown in Fig. 3.10. The figure clearly shows the shift of the peak positions with the Ca composition x.

In order to analyze the structural change in the formed crystallites with the Ca compositions, the lattice constants of the crystalline film samples were evaluated by assuming cubic structures for the crystallites. For the samples with $x = 0$, 0.25, 0.50 and 0.75, the evaluation was performed from the angles of 110, 200 and 211 diffraction peaks in cubic structure by using CellCalc [13], and that of the $x = 1$ sample was estimated as the cube root of the lattice volume evaluated by CellCalc from the angles of 101, 200, 121, 002 and 202 diffraction peaks in orthorhombic structure. The estimated lattice constants are plotted as a function of the Ca composition x in Fig. 3.11 and listed in Table 3.4. The lattice constants a showed continuous and rather linear relation to x. The continuity and the fact that no phase separation was observed in the samples evidence the formation of monophasic $Ba_{1-x}Ca_xZrO_3$ solid solutions without miscibility gap between

Ba^{2+} and Ca^{2+} ions, and the linear relation indicates that the formed crystalline film samples have the same compositions of the targets used in the sputtering according to Vegard's law.

Fig. 3.12 shows SEM images of the $x = 0.50$ target and the annealed film sample formed by using the target along with the two-dimensional elemental mappings corresponding to the SEM images for Ba and Ca by the EDX analyses. In the target, the existence of Ba-rich and Ca-rich phases as the result of the phase separation was observed clearly. On the other hand, the results of the EDX analysis demonstrated homogeneous distributions of Ba and Ca in the annealed film sample supporting the formation of $Ba_{0.50}Ca_{0.50}ZrO_3$ solid solution.

The annealing at the rather low temperature of 800 °C is considered to allow only short-range diffusion of the ions in the amorphous samples. Such diffusion is, however, enough for the amorphous samples to crystallize because of the homogeneous dispersion of the constituent ions and the continuous structure as the characteristics of amorphous. The $Ba_{1-x}Ca_xZrO_3$ solid solutions are considered to be formed in such a way without phase separation, which occurs through long-range diffusion of the ions.

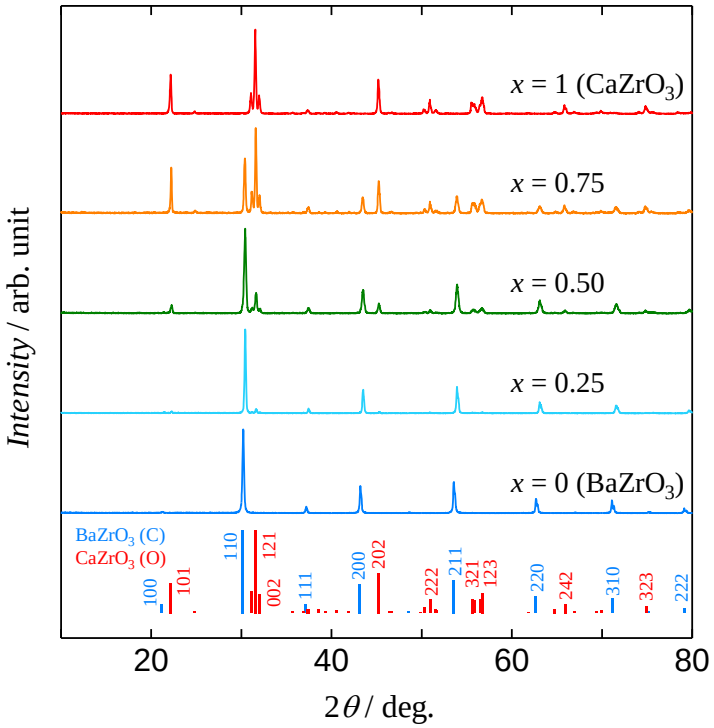

Fig. 3.2 XRD patterns of the $Ba_{1-x}Ca_xZrO_3$ targets.

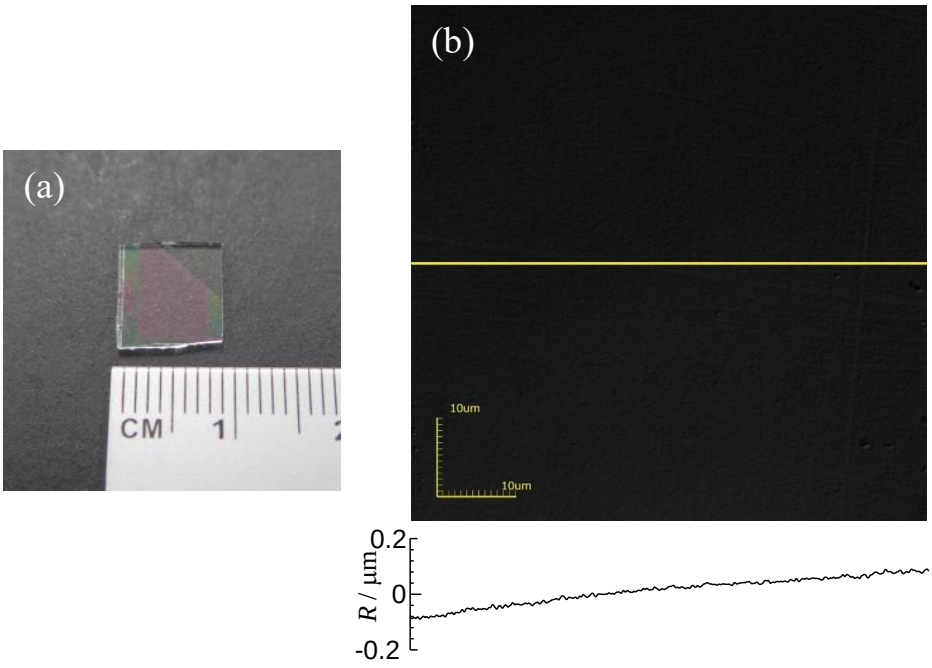

Fig. 3.3 As-prepared film sample deposited on the quartz glass substrate by the sputtering with using the $(BaZrO_3)_{0.50}(CaZrO_3)_{0.50}$ target; (a) photograph of the sample, (b) surface image and roughness profile observed by laser scanning microscope. Surface roughness, *R*, was measured along the yellow line indicated in the image.

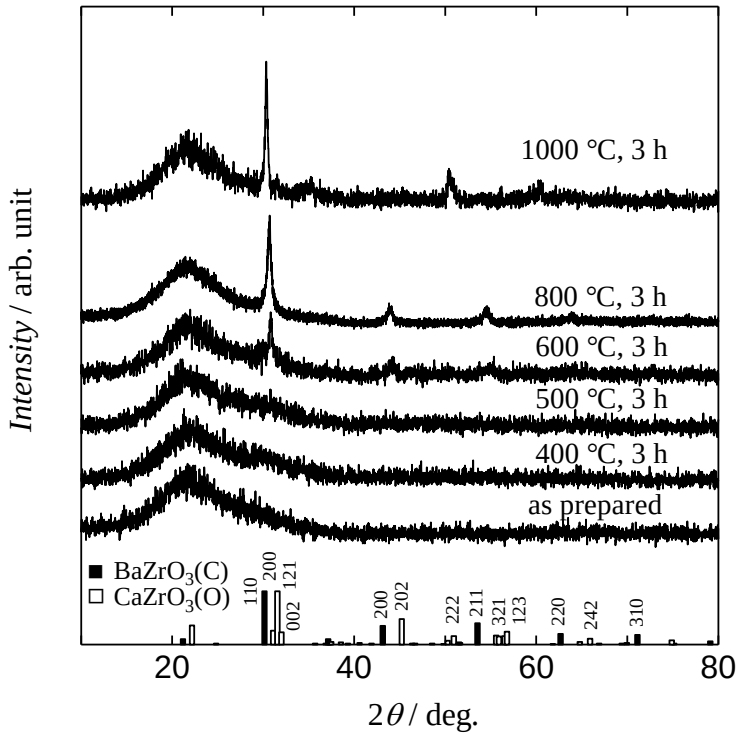

Fig. 3.4　XRD pattern of the film sample deposited on the quartz glass substrate by the sputtering using the $(BaZrO_3)_{0.50}(CaZrO_3)_{0.50}$ target, and those of the samples after annealing.

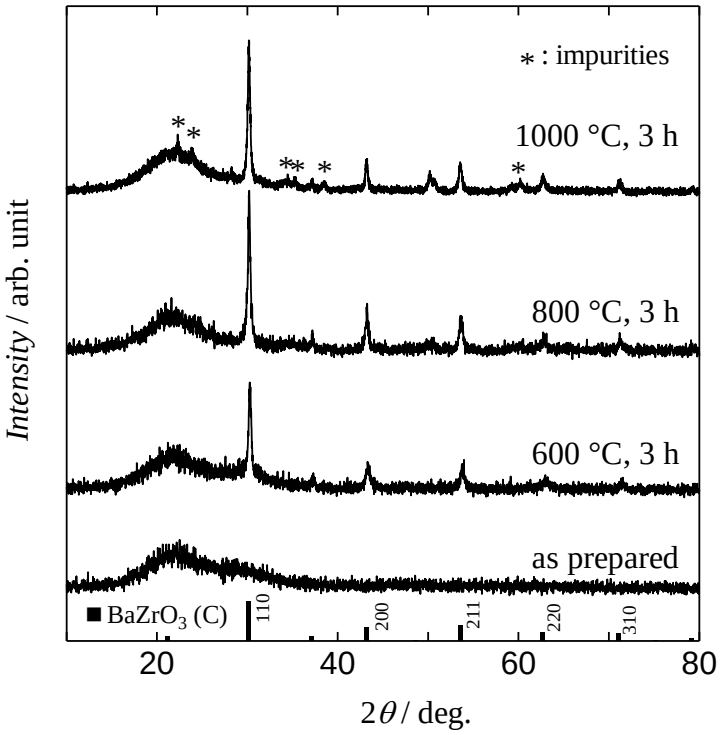

Fig. 3.5 XRD pattern of $BaZrO_3$ film sample deposited on the quartz glass substrate by the sputtering, and those of the samples after annealing.

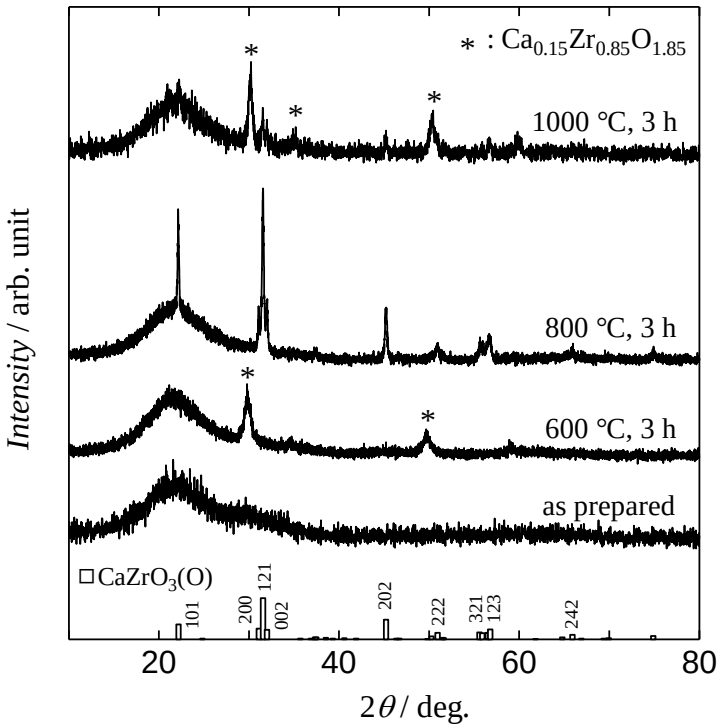

Fig. 3.6　XRD patterns of $CaZrO_3$ film sample deposited on the quartz glass substrates by the sputtering, and those of the samples after annealing.

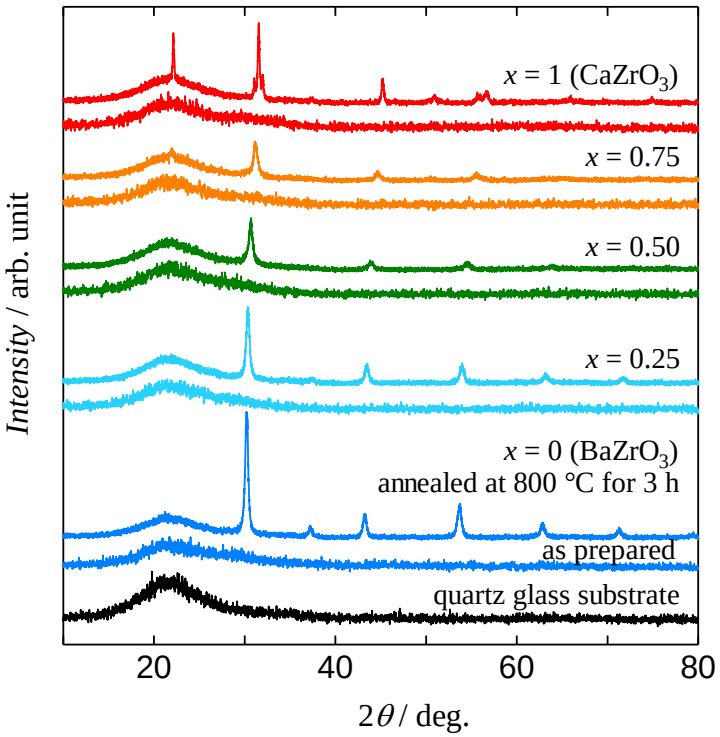

Fig. 3.7 XRD patterns of the as-prepared film samples by the rf magnetron sputtering and the annealed $Ba_{1-x}Ca_xZrO_3$ film samples along with that of the quartz glass substrate.

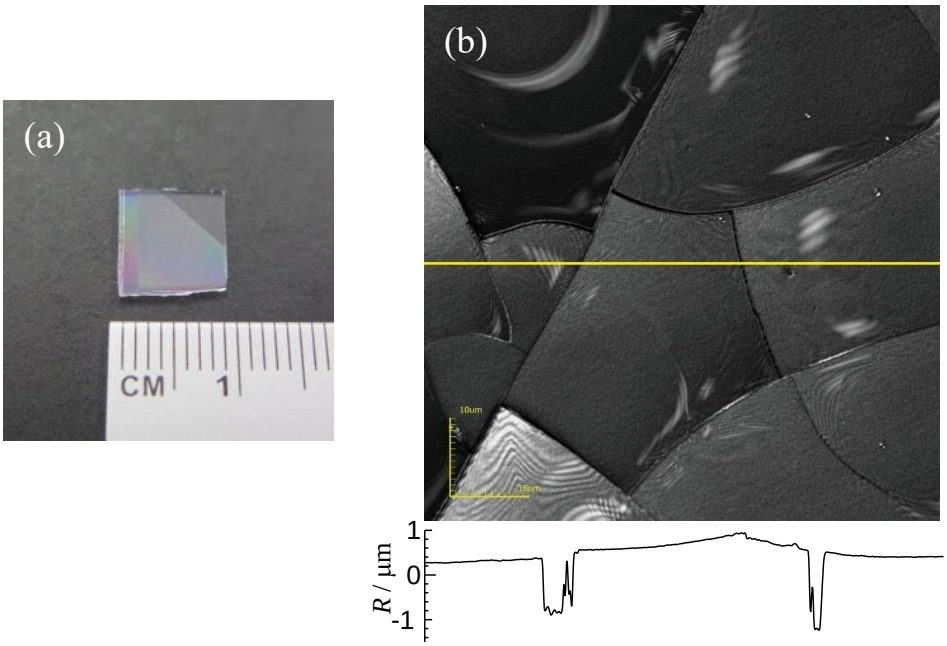

Fig. 3.8　Annealed film sample formed on the quartz glass substrate by the sputtering with using the $(BaZrO_3)_{0.50}(CaZrO_3)_{0.50}$ target; (a) photograph of the sample, (b) surface image and roughness profile observed by laser scanning microscope. Surface roughness, *R*, was measured along the yellow line indicated in the image.

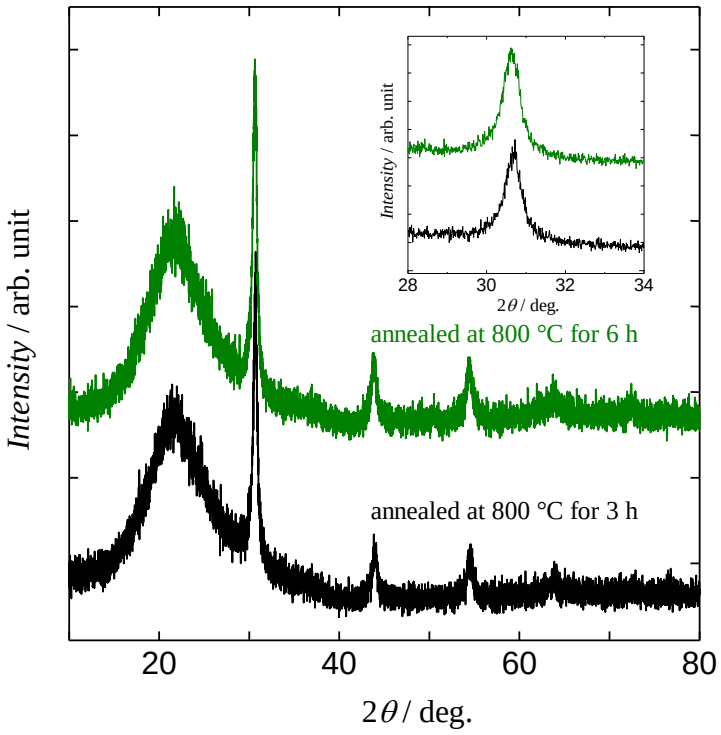

Fig. 3.9 XRD patterns of the $Ba_{0.50}Ca_{0.50}ZrO_3$ film samples annealed at 800 °C for 3 h (black line) and 6 h (green line). Inset is an enlarged view of the diffractions around 2θ = 32°.

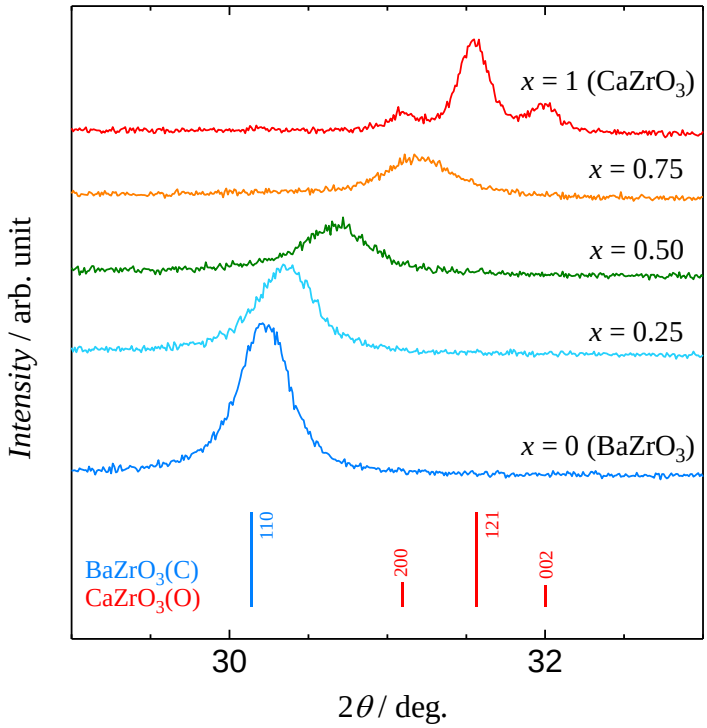

Fig. 3.10 Enlarged view of the X-ray diffractions of the annealed $Ba_{1-x}Ca_xZrO_3$ film samples.

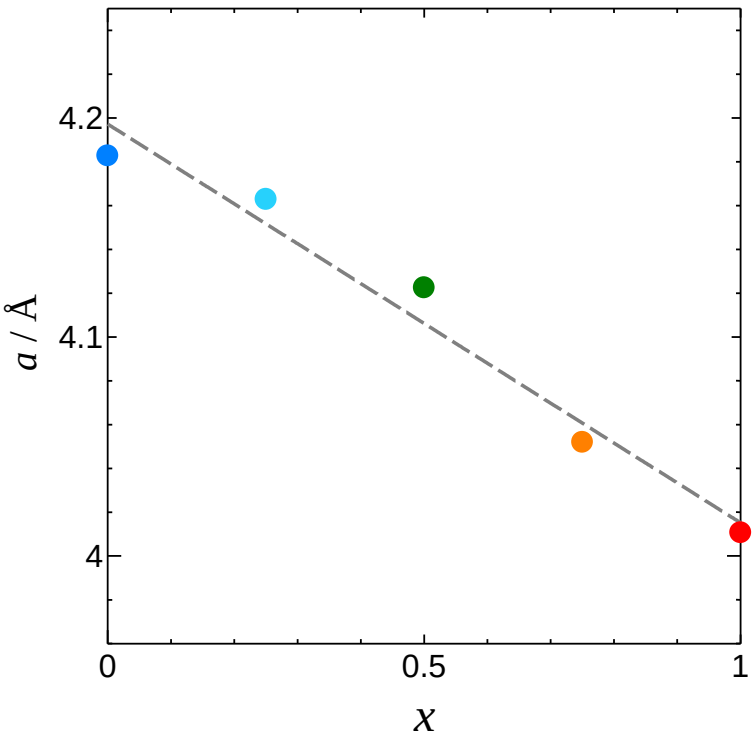

Fig. 3.11 Dependence of the lattice constants *a* of the crystalline film samples on the Ca composition *x*.

Table 3.4 Mole fraction of $CaZrO_3$ in $Ba_{1-x}Ca_xZrO_3$ solid solutions x, and experimental values of lattice constants a of the solid solutions at temperature T = 298.15 K and pressure p = 0.1 MPa,[a] and standard uncertainties u of x and a

x	a / Å	$u(x)$	$u(a)$ / Å
0 ($BaZrO_3$)	4.183	--	0.0119
0.25	4.163	0.060	0.0119
0.50	4.123	0.060	0.0119
0.75	4.052	0.060	0.0119
1 ($CaZrO_3$)	4.011*	--	0.0119

[a] Standard uncertainties u are $u(T)$ = 1 K and $u(p)$ = 10 kPa.

* The lattice constants for $CaZrO_3$ sample were assessed to be a = 5.749 Å, b = 8.022 Å, c = 5.596 Å and V = 258.1 $Å^3$ in orthorhombic structure, and the lattice constant a on the assumption of cubic structure was evaluated as the cube root of the lattice volume V in orthorhombic structure.

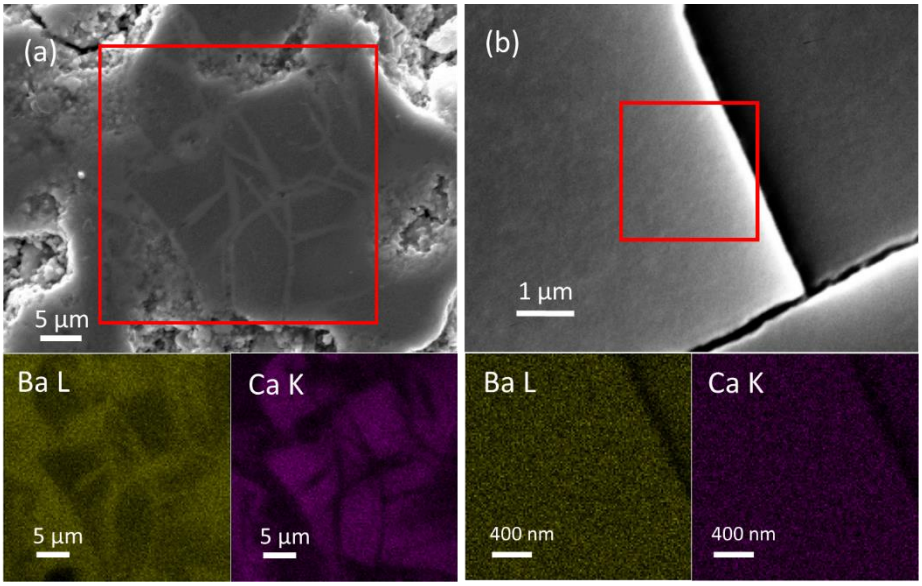

Fig. 3.12 SEM images and elemental mappings corresponding to the areas indicated by red squares in the SEM images for Ba and Ca of the $Ba_{0.50}Ca_{0.50}ZrO_3$ target (a) and the annealed film sample formed by using the target (b).

3.3.2. Dielectric properties of $Ba_{1-x}Ca_xZrO_3$ solid solutions

To obtain the information about the dielectric properties of $Ba_{1-x}Ca_xZrO_3$ solid solutions, I examined the formation of the solid-solution film samples on Nb(1.0 wt%)-doped $SrTiO_3$ single crystals ($SrTiO_3$:Nb; Furuuchi Chemical, 10 mm × 10 mm × 0.5 mm*t* with (100) polished plane), which have electric conductivity of ~400 S cm^{-1}, in the same manner as on the quartz glass substrate. A photograph of the as-prepared film sample formed on the $SrTiO_3$:Nb substrate by the sputtering with using the $(BaZrO_3)_{0.50}(CaZrO_3)_{0.50}$ target is shown in Fig. 3.13(a). Fig. 3.13(b) is a surface image and roughness profile of the as-prepared film sample observed by the laser scanning microscope. As shown in Fig. 3.13(b), the surface of the film sample is uneven slightly but rather flat without crack. As-prepared film samples exhibited halo patterns at around $2\theta = 30°$ in the XRD experiments as shown in Fig.3.14, and were confirmed to have amorphous structure as in the cases using the quartz glass substrates.

To form the $Ba_{1-x}Ca_xZrO_3$ solid solutions on the $SrTiO_3$:Nb single-crystal substrates, I annealed the amorphous film samples at 800 °C for 3 h. XRD results of the annealed samples are shown in Fig. 3.15. Crystallization of the samples proceeded by the annealing also on the substrates, and the peaks shifted continuously to higher angles with the Ca composition *x* without showing splitting. The XRD results indicate the formation of $Ba_{1-x}Ca_xZrO_3$ solid solutions in whole the Ca composition range of $0 \leq x \leq 1$ without phase separation nor the formation of byproduct on the $SrTiO_3$:Nb single crystals. Fig. 3.16(a) is a photograph of the annealed $Ba_{0.50}Ca_{0.50}ZrO_3$ film sample formed on the $SrTiO_3$:Nb single crystal substrate, and Fig. 3.16(b) is a surface image and roughness profile of the annealed film sample observed by the laser scanning microscope. No crack

was observed in the annealed sample on the $SrTiO_3$:Nb single-crystal substrate differently from that on the quartz glass substrate by the matching of thermal expansion coefficients between the film sample and the substrate [12,14], and the roughness of the surface of the samples was estimated to be within ±25 nm.

Dielectric measurements were performed by using the substrate as an electrode and prepare a Pt counter electrode (1.7 × 1.7 mm^2) on the surface of each sample by sputtering. As shown in Fig. 3.17, no significant change was observed in the dielectric constants ε with frequency in each sample within the measured frequency range 10^2–10^5 Hz, and the evaluated ε for the $x = 0$ ($BaZrO_3$) sample agreed with the reported value [15] within the estimated experimental error.

The evaluated values of ε at 1 kHz for the samples are listed in Table 3.5, and the Ca composition dependence of ε is shown in Fig. 3.18(a). The constants ε decreased linearly with the Ca composition x. The observed dependence of ε on the Ca composition is different from that in $Ba_{1-x}Ca_xTiO_3$ solid solutions, in which ε changes convexly with Ca composition. The peculiar Ca composition dependence of the permittivity in $Ba_{1-x}Ca_xTiO_3$ solid solutions has been understood to originate in the space produced around Ca^{2+} ions by the mixing of Ba^{2+} and Ca^{2+} ions, which allow larger displacement of Ti^{4+} ions responding to the applied electric field. In the $Ba_{1-x}Ca_xZrO_3$ solid solutions, only the L(Ca–O) in the samples with $x = 0.25$, 0.50, 0.75 and 1 were found to have larger values than the sum of the ionic radii of the metal and oxygen ions as in the case of $Ba_{1-x}Ca_xTiO_3$ solid solutions. The magnitude of the extra space around Ca^{2+} ions in the samples can be expressed as ΔL, which was evaluated by subtracting the ionic radii of Ca^{2+} and O^{2-} from the L(Ca–O). The value of ΔL multiplied by the Ca composition x, $\Delta L \times x$, for the $Ba_{1-x}Ca_xZrO_3$ solid solutions indexes the amount of the extra space in the

crystalline lattice of the sample. As shown in Fig. 3.18(b), the value of $\Delta L \times x$ shows a tendency to increase with the mixing of Ba^{2+} and Ca^{2+} ions and exhibits a maximum at around $x = 0.9$. However, such a tendency in the Ca composition dependence of the permittivities was not observed in the $Ba_{1-x}Ca_xZrO_3$ solid solutions.

The origin of the difference in the Ca composition dependences between the titanate and the zirconate is not clear at this stage. However, Shannon's ionic radii of Zr^{4+} and Ti^{4+} ions are 0.720 Å and 0.605 Å, respectively [16], and the difference in the Ca composition dependences of the permittivities is considered to be due to the larger size of Zr^{4+} ion than Ti^{4+} ion, which restricts the displacement of Zr^{4+} ions in the crystalline lattice as shown in Fig. 3.19. The results also indicate that the Ca composition dependence of ε in $Ba_{1-x}Ca_xTiO_3$ solid solutions is affected more seriously by the displacement of Ti^{4+} ions than that of Ca^{2+} ions.

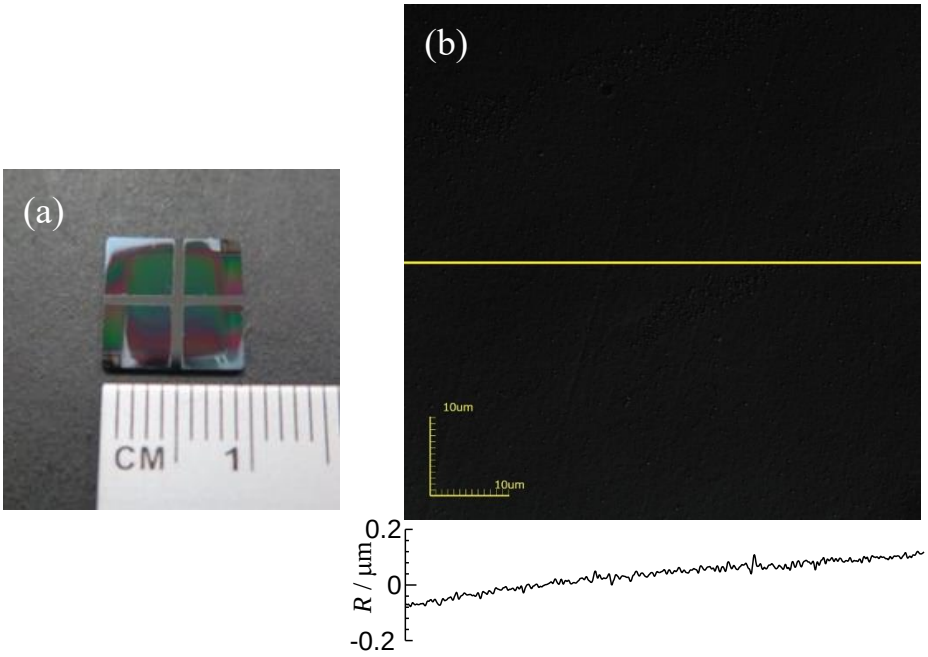

Fig. 3.13 As-prepared film sample deposited on the $SrTiO_3$:Nb substrate by the sputtering with using the $(BaZrO_3)_{0.50}(CaZrO_3)_{0.50}$ target; (a) photograph of the sample, (b) surface image and roughness profile observed by laser scanning microscope. Surface roughness, *R*, was measured along the yellow line indicated in the image.

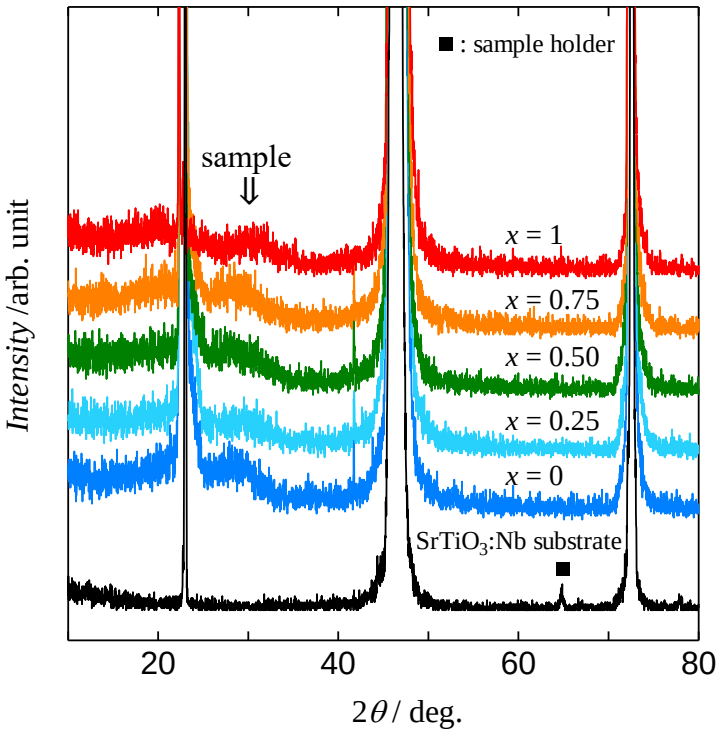

Fig. 3.14 XRD patterns of the as-prepared film samples formed by the rf magnetron sputtering with using the $(BaZrO_3)_{1-x}(CaZrO_3)_x$ targets and that of the $SrTiO_3$:Nb single crystals used as the substrates.

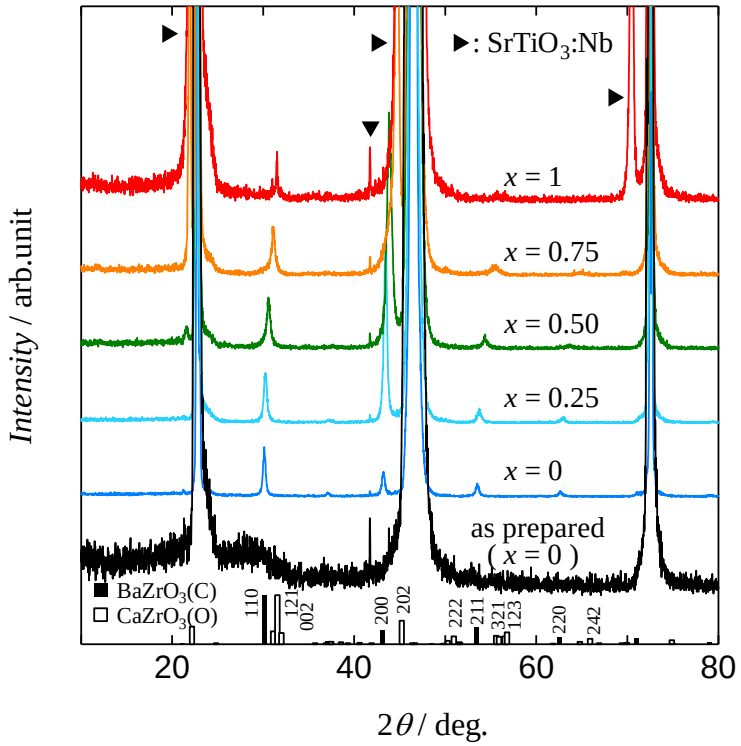

Fig. 3.15 XRD patterns of the annealed film samples formed on the $SrTiO_3$:Nb single-crystal substrates by the sputtering with using the $(BaZrO_3)_{1-x}(CaZrO_3)_x$ targets.

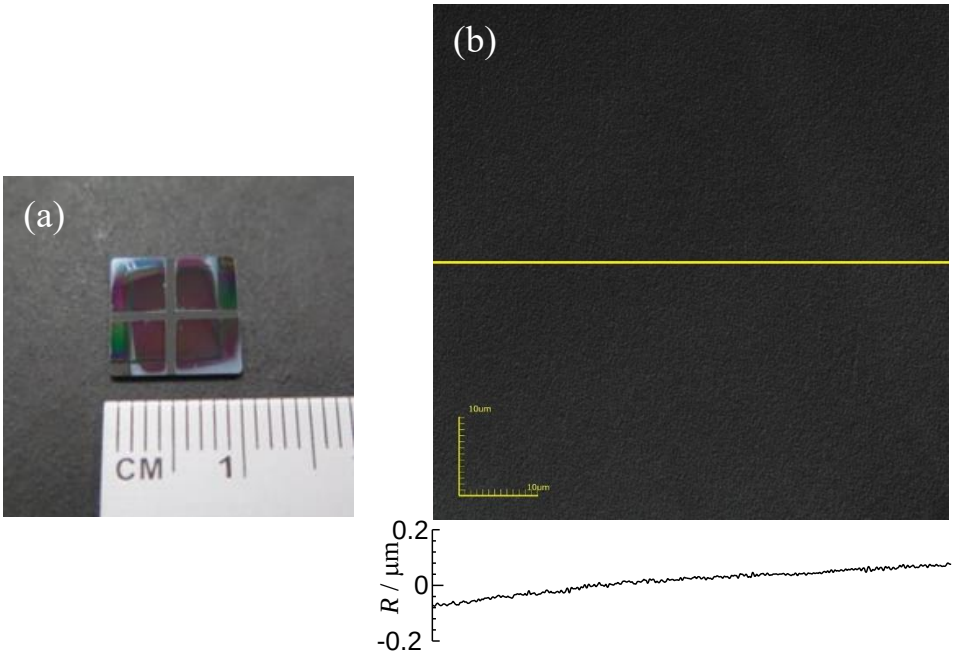

Fig. 3.16 Annealed film sample formed on $SrTiO_3$:Nb substrate by the sputtering with using the $(BaZrO_3)_{0.50}(CaZrO_3)_{0.50}$ target; (a) photograph of the sample, (b) surface image and roughness profile observed by laser scanning microscope. Surface roughness, *R*, was measured along the yellow line indicated in the image.

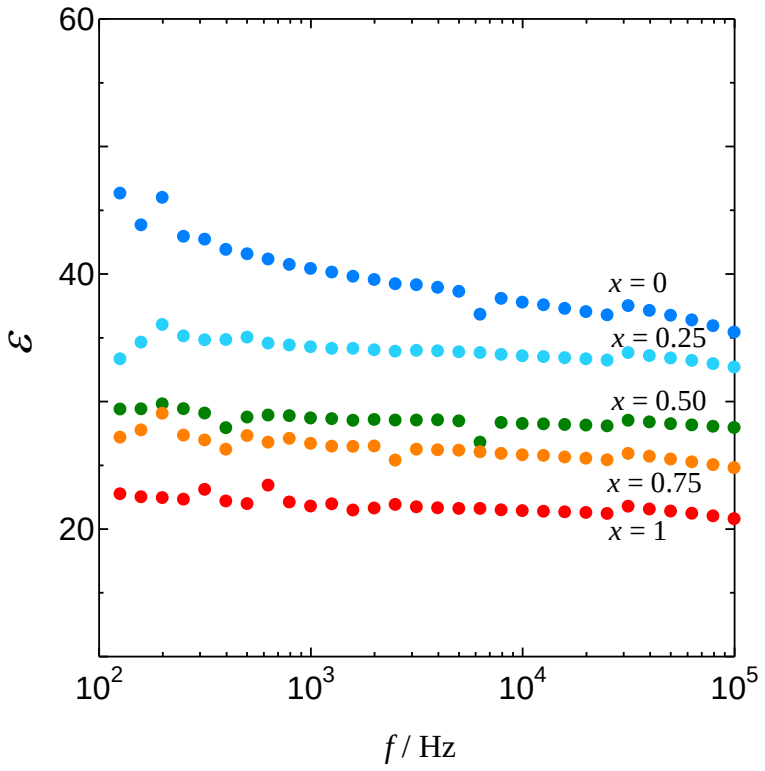

Fig. 3.17　Frequency dependence of the dielectric constants ε of $Ba_{1-x}Ca_xZrO_3$ solid-solution film samples.

Table 3.5 Mole fraction of $CaZrO_3$ in $Ba_{1-x}Ca_xZrO_3$ solid solutions x, and experimental values of dielectric constants ε at frequency ν = 1 kHz with oscillating electric field E = 10 mV_{rms} of the solid solutions at temperature T = 298.15 K and pressure p = 0.1 MPa,[a] and standard uncertainties u of x and ε

x	ε	$u(x)$	$u(\varepsilon)$
0 ($BaZrO_3$)	45.2	--	4.98
0.25	39.1	0.060	4.35
0.50	35.0	0.060	4.22
0.75	27.9	0.060	2.36
1 ($CaZrO_3$)	22.8	--	0.68

[a] Standard uncertainties u are $u(\nu)$ = 100 mHz, $u(E)$ = 20 μV_{rms}, $u(T)$ = 1 K and $u(p)$ = 10 kPa.

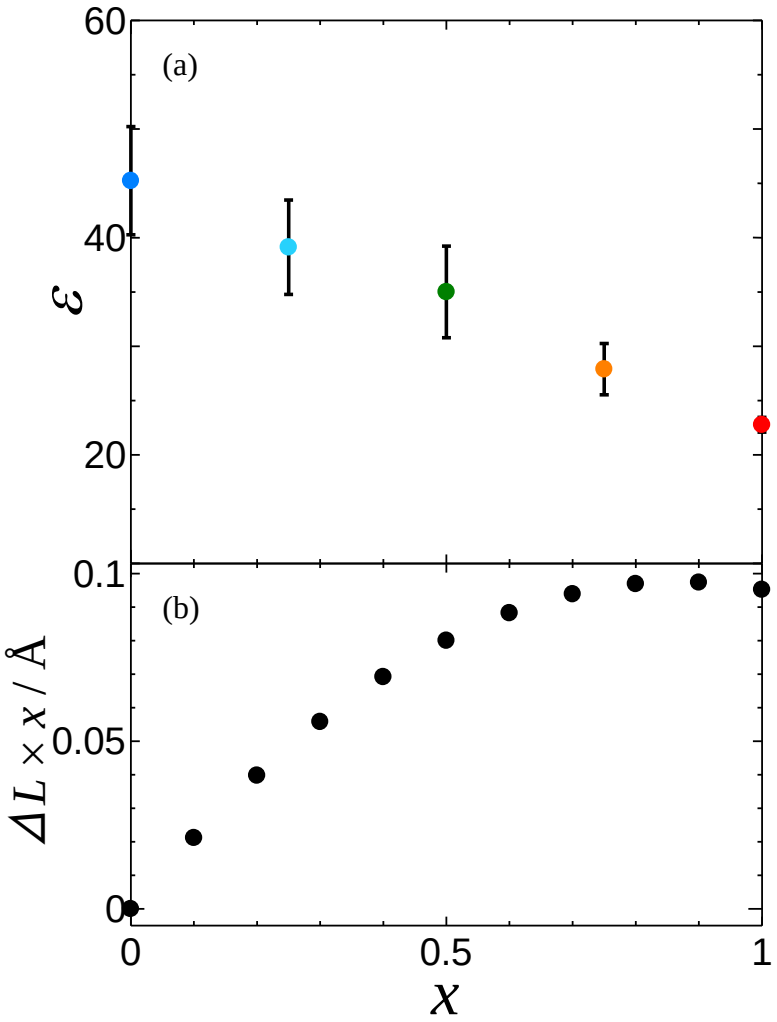

Fig. 3.18 Dielectric constants ε at 1 kHz of the $Ba_{1-x}Ca_xZrO_3$ solid-solution samples (a), and Ca composition x dependence of the extra space around Ca^{2+} ions in the $Ba_{1-x}Ca_xZrO_3$ solid solutions of $\Delta L \times x$ (b). Error bars in (a) represent the standard deviations of the ε evaluated from the results for separately prepared several samples, and the $\Delta L \times x$ value for $x = 0$ in (b) was estimated by putting Ca^{2+} ion in the Ba^{2+}-ion site imaginarily.

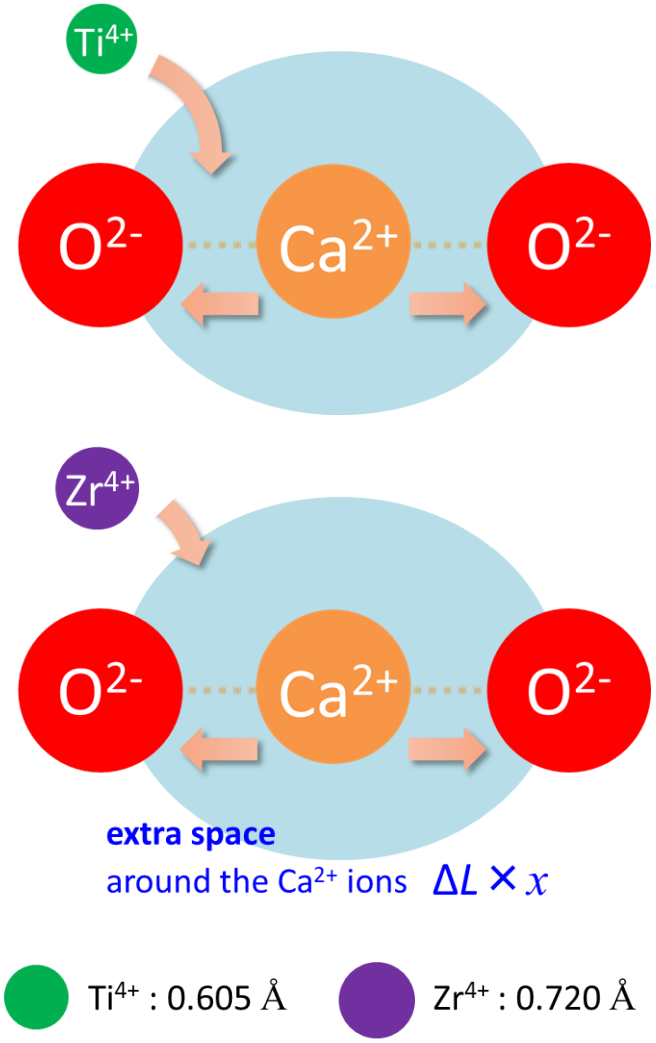

Fig. 3.19 Schematic illustration of the displacement of the Ti^{4+} and Zr^{4+} ions in $Ba_{1-x}Ca_xTiO_3$ and $Ba_{1-x}Ca_xZrO_3$ solid solutions.

3.4. Conclusions

In this work, I succeeded in forming $Ba_{1-x}Ca_xZrO_3$ solid solutions in whole the Ca composition range despite the narrow solubility limit in the system. The formation of the solid solutions demonstrates the usefulness and the validity of the sputter-anneal method for the formation of solid solutions in perovskite-type oxides. It should be noted that the attempts to form $CaZrO_3$ film samples by rf magnetron sputtering and laser ablation onto heated substrates have been reported to result in the formation of calcia-stabilized zirconia besides $CaZrO_3$ [6,10]. Nevertheless, $CaZrO_3$ crystalline film sample was obtained here without the formation of byproducts by the sputter-anneal method, indicating the usefulness of the method also for the preparation of the crystalline film samples in perovskite-type compounds.

References

[1] M. Lorenz *et al*., The 2016 oxide electronic materials and oxide interfaces roadmap, J. Phys. D: Appl. Phys. 49 (2016) 433001. https://doi.org/10.1088/0022-3727/49/43/433001

[2] I. Levin, T. G. Amos, S. M. Bell, L. Farber, T. A. Vanderah, R. S. Roth, B. H. Toby, Phase equilibria, crystal structures, and dielectric anomaly in the $BaZrO_3$-$CaZrO_3$ system, J. Solid State Chem. 175 (2003) 170–181. https://doi.org/10.1016/S0022-4596(03)00220-2

[3] T. Yamaguchi, Y. Komatsu, T. Otobe, Y. Murakami, Newly Developed Ternary (Ca,Sr,Ba) Zirconate Ceramic System for Microwave Resonators, Ferroelectrics 27 (1980) 273–276. https://doi.org/10.1080/00150198008226116

[4] J. W. Bennett, I. Grinberg, A. M. Rappe, Nonmonotonic Composition Dependence of the Dielectric Response of $Ba_{1-x}Ca_xZrO_3$, Chem. Mater. 20 (2008) 5134–5138. https://doi.org/10.1021/cm800929e

[5] A. Cimino, F. S. Stone, Oxide Solid Solutions as Catalysts, Adv. Catal. 47 (2002) 141–306. https://doi.org/10.1016/S0360-0564(02)47007-1

[6] M. Joseph, N. Sivakumar, P. Manoravi, S. Vanavaramban, Preparation of thin film of $CaZrO_3$ by pulsed laser deposition, Solid State Ionics 144 (2001) 339–346. https://doi.org/10.1016/S0167-2738(01)00971-7

[7] L. A. Dunyushkina, S. V. Plaksin, A. A. Pankratov, L. A. Kuz'mina, V. M. Kuimov, V. P. Gorelov, Synthesis and Properties of $CaZrO_3$ Films on YSZ Electrolyte Surface, Russ. J. Electrochem. 47 (2011) 1274–1280. https://doi.org/10.1134/S102319351111005X

[8] P. Gonon, F. E. Kamel, Dielectric response of Cu/amorphous $BaTiO_3$/Cu capacitor, J. Appl. Phys. 101 (2007) 073901. https://doi.org/10.1063/1.2716871

[9] M. Ako, T. Kogure, Y. Kobayashi, T. Kyomen, J. Fujisawa, M. Hanaya, Formation of $Ba_{1-x}Ca_xTiO_3$ solid solutions beyond the solubility limit by 'sputter-anneal' method, Thermochim. Acta 679 (2019) 178339. https://doi.org/10.1016/j.tca.2019.178339

[10] J. -S. Kim, J. -M. Han, M. -R. Joung, S. -H. Kweon, C. -Y. Kang, J. -H. Paik, Y. -H. Jeong, S. Nahm, $Ca_{0.15}Zr_{0.85}O_{1.85}$ Thin Film for Application to MIM Capacitor on Organic Substrate, Energy Harv. Sys. 1 (2014) 243–250. https://doi.org/10.1515/ehs-2014-0010

[11] NEOTRON CO., LTD, http://www.neotron.co.jp/crystal/1/BaTiO3.html

[12] Shin-Etsu Quartz Products Co., Ltd., Technology Guide 1 (2018) p. 8. https://www.sqp.co.jp/catalog/images/Technology_Guide1_j.pdf

[13] H. Miura, CellCalc: A unit cell parameter refinement program on Windows computer, J. Cryst. Soc. Jpn. 45 (2003) 145–147. https://doi.org/10.5940/jcrsj.45.145

[14] Furuuchi Chemical, http://www.furuchi.co.jp/crystal/srtio3.html

[15] G. Lupina *et al*., Dielectric constant and leakage of $BaZrO_3$ films, Appl. Phys. Lett. 94 (2009) 152903. https://doi.org/10.1063/1.3110970

[16] R. D. Shannon, Revised effective ionic radii and systematic studies of interatomic distances in halides and chalcogenides, Acta Cryst. A 32 (1976) 751–767. https://doi.org/10.1107/S0567739476001551

Chapter 4. Summary

In this study, I tried to expand the solubility limit in perovskite-type oxide systems of $BaTiO_3$−$CaTiO_3$ and $BaZrO_3$−$CaZrO_3$, and also investigated composition dependence of the permittivity in the formed solid solutions.

In the $BaTiO_3$−$CaTiO_3$ system, I succeeded in forming $Ba_{1-x}Ca_xTiO_3$ solid solutions beyond the solubility limit reported so far by applying the 'sputter-anneal' method, in which amorphous film samples were prepared by rf magnetron sputtering and annealed subsequently at a moderate temperature condition. The amorphous film samples were observed to crystallize at lower temperatures than those applied in a conventional solid-state reaction, which allows only a restricted migration of constituent ions and suppresses the proceeding of phase separations resulting in the formation of solid solutions. Because the amorphous sample having high fictive temperature was annealed at a moderate temperature, the solid solution was considered to be formed effectively as the product in a meta-stable phase. The dielectric constants ε of the formed solid solutions $Ba_{1-x}Ca_xTiO_3$ were observed to increase with the mixing of Ba^{2+} and Ca^{2+} ions, and the sample with $x = 0.35$ showed the highest dielectric constant. This peculiar dependence of the ε on the Ca composition x was well explained by the formation of extra space around Ca^{2+} ions substituted for Ba^{2+} ions, and the displacements of Ca^{2+} and probably Ti^{4+} ions using the space were understood to affect largely the dielectric properties of $Ba_{1-x}Ca_xTiO_3$ solid solutions.

Also in the $BaZrO_3$−$CaZrO_3$ system, I succeeded in forming $Ba_{1-x}Ca_xZrO_3$ solid solutions in whole the Ca composition range despite the narrow solubility limit in the system. The formation of the solid solutions demonstrates the usefulness and the validity of the sputter-anneal method for the formation of solid solutions in perovskite-type oxides. Although the attempts to form $CaZrO_3$ film samples by rf magnetron sputtering and laser ablation onto heated substrates have been reported to result in the formation of calcia-stabilized zirconia besides $CaZrO_3$, $CaZrO_3$ crystalline film sample was obtained here without the formation of byproducts by the sputter-anneal method. This fact emphases the usefulness of the method in preparing crystalline film samples of perovskite-type compounds.

The dielectric constants ε of the $Ba_{1-x}Ca_xZrO_3$ solid solutions decreased linearly with the Ca composition x differently from those in the $Ba_{1-x}Ca_xTiO_3$ solid solutions, in which the dielectric constants ε change convexly with Ca composition. The origin of the difference in the Ca composition dependences between the titanate and the zirconate is not clear at this stage. However, the difference of the sizes of Ti^{4+} and Zr^{4+} ions is considered possible to affect the dependence and molecular dynamics (MD) simulations to estimate the degree of the displacement of ions under electric field for $Ba_{1-x}Ca_xTiO_3$ and $Ba_{1-x}Ca_xZrO_3$ solid solutions will gain an insight into this issue.

The sputter-anneal method developed in this study would produce new solid-solution materials in perovskite-type oxide systems and possibly in some other kinds of oxide systems. I hope such works bring us a more precise understanding of the property dependences of oxide solid solutions on the compositions, which might allow detailed controlling of the properties more effectively.

Acknowledgements

First of all, I express sincere gratitude to Professor Minoru Hanaya of Gunma University, who provides a lot of advice and encouragement. I am deeply grateful to Professor Hanaya, again, for his continuous support and trust in me.

I am very grateful to Professor Jun-ichi Fujisawa of Gunma University for his helpful advice.

I would like to say an extended thanks to Professor Toru Kyomen of Gunma University for his helpful discussion.

I thank Mr. K. Sakamoto of the Center for Instrumental Analysis of Gunma University for his technical assistance in the SEM-EDX experiment. The XRD and SEM-EDX experiments were performed using instruments at the Center for Instrumental Analysis of Gunma University.

I wish to thank Professor Soshi Shiraishi, Professor Naoki Asakawa, Professor Seiji Tobita, Professor Shinji Iwamoto, Professor Jun-ichi Fujisawa, and Professor Minoru Hanaya for supplying useful information and making helpful comments during the preparation of this doctoral dissertation.

I would like to acknowledge the Grant for Doctor-Course Student in Domain of Materials and Bioscience (Graduate School of Science and Technology, Gunma University) and the support for a research assistant (Academic-Industrial Collaboration, Human Resources Cultivation Center, Gunma University), which have supported this doctoral research work.

I would like to warmly thank all the members of Physical Science Laboratory of Gunma University. I have enjoyed a great and precious time with them.

Finally, I would like to share the satisfaction of this achievement with my family, and I really thank their help and support.

Miho Ako (阿光 美歩)